Morphological Characterization of Microporous Layers for Polymer Electrolyte Fuel Cells

by

Abhishek Nanjundappa

M.Sc., Chalmers University of Technology, 2008

B.Eng., Visvesvaraya Technological University, 2005

Thesis Submitted in Partial Fulfillment of the

Requirements for the Degree of

Master of Applied Science

in the

School of Mechatronic Systems Engineering

Faculty of Applied Sciences

SIMON FRASER UNIVERSITY

Summer 2022

Declaration of Committee

Name:	**Abhishek Nanjundappa**
Degree:	**Master of Applied Science**
Title:	**Morphological Characterization of Microporous Layers for Polymer Electrolyte Fuel Cells**
Committee:	**Chair:** **Ahad Armin** Lecturer, Mechatronic Systems Engineering
	Erik Kjeang Supervisor Professor, Mechatronic Systems Engineering
	Frank Orfino Committee Member Research Associate, Mechatronic Systems Engineering
	Kourosh Malek Committee Member Head of Division Artificial Materials Intelligence Forschungszentrum Juelich
	Krishna Vijayaraghavan Examiner Associate Professor, Mechatronic Systems Engineering

Abstract

The microporous layer (MPL) in polymer electrolyte fuel cells is known to enhance performance and durability of the membrane electrode assembly. However, the design and functional understanding of the MPL has been predominantly empirical to date, as its key structural parameters and transport properties are difficult to determine due to the lack of MPL-specific measurement techniques. The present work aims to establish a specialized framework for 3-D image based morphological characterization for two types of MPL materials using carbon black (CB) nanoparticles and graphite particles. The proposed framework features a tuned focused ion beam-scanning electron microscope (FIB-SEM) imaging technique and an in-house developed procedure for image processing and reconstruction of the true 3-D structure which is validated with measured porosimetry data for a pure MPL sample. The effects of FIB milling parameters are evaluated and tuned to prevent image bias and damage to the delicate MPL structure. The pore size distribution of the reconstructed MPL structure is determined using a modified algorithm based on 3-D Euclidian distance transform (EDT) and the results are found to be in good agreement with the measured data. The 3-D reconstructed models containing the structural information are utilized as numerical domains for calculation of key MPL material properties, namely effective diffusivity, tortuosity, and effective thermal conductivity. By comparing the obtained material properties in the through-plane and in-plane directions, the CB MPL is determined to be isotropic, the fine graphite particle MPL to be transversely isotropic and the coarse graphite particle to be anisotropic. The obtained material properties are useful in the areas of modeling, material development, and membrane electrode assembly (MEA) design.

Keywords: Polymer electrolyte fuel cell; Microporous layer; Gas diffusion layer; Focused ion beam-scanning electron microscope; Characterization

To Mom and Dad, Sister and all my loved ones

Acknowledgments

I would like to express my sincere gratitude towards following persons for their contributions. There are myriad of people who made this thesis possible, only some of whom I have space to name here.

First and foremost, I would like to thank my senior supervisor, Dr. Erik Kjeang. We first met when he visited KTH, Sweden as a guest speaker and I had the privilege to host him. Took a leap of faith and decided to start my graduate degree in Canada. It has been a long journey with ups and lots of downs. I am grateful for his patience and support during the time I spent at SFU.

To Frank Orfino and Dr. Kourosh Malek for serving as my committee members and supplying valuable technical input. I am thankful to Dr Krishna Vijayaraghavan for the evaluation of this thesis.

To Dr. Mohamed El Hannach for writing the modified algorithm that finds the 3-D Euclidian distance transform (EDT). Dr Alireza Sadeghi for image acquisition and image processing of fine graphite (FG) and coarse graphite (CG) MPL samples.

To Ballard Power Systems, industrial collaborator. Specifically, Dr. David Harvey, Julie Bellerive, and Shanna Knights; for their time, cooperation, and technical input.

To 4D LABS, SFUs shared facilities supported by the Canada Foundation for Innovation (CFI), British Columbia Knowledge Development Fund (BCKDF), Western Economic Diversification Canada (WD) and Simon Fraser University (SFU).

To all my great friends in TSSU, GSS, and SFPIRG, for your camaraderie and friendship. Special shout-out to Jorji (5063), Derek (softball), Harjap (grassroots resistance), Amal, Yadvinder, Rahil (MSU), Teresa (housing), Christina, Melissa, Lillian, Anthony (AK47, 3204), and Jade (WT).

To my most remarkable parents and sister, for your unconditional love, and for your endless support that can be felt over 12 000 km away. I love you dearly.

Table of Contents

List of Tables

List of Figures

List of Acronyms

ACL	Anode catalyst layer
BP	Bipolar plate
CB	Carbon black
CCL	Cathode catalyst layer
CCM	Catalyst coated membrane
CG	Coarse graphite
CL	Catalyst layer
CNN	Convolutional neural network
CVF	Cumulative volume fraction
DB	Dual beam
DPV	Differential pore volume
EDT	Euclidian distance transform
FEI	Field electron and Ion
FEM	Finite element method
FG	Fine graphite
FIB-SEM	Focused ion beam – Scanning electron microscopy
GDL	Gas diffusion layer
HOR	Hydrogen oxidation reaction
HVAC	Heating ventilation and air-conditioning
IP	In-plane
MEA	Membrane electrode assembly
MIP	Mercury intrusion porosimetry
MPL	Micro porous layer
OCV	Open circuit voltage
ORR	Oxygen reduction reaction
PEM	Polymer electrolyte membrane
PSD	Pore size distribution
PTFE	Polytetrafluoroethylene
RH	Relative humidity
SD	Sectioning directions
SOFC	Solid oxide fuel cells
TEM	Transmission electron microscopy

TP	Through-plane
XCT	X-ray computed tomography

Nomenclature

Greek symbols

Symbol	Description	Unit
α	Bruggeman exponent	
γ	Effective diffusivity	
ε	Porosity	
θ	Off-normal viewing angle	^{o}
ϕ	Contact angle	^{o}
ψ	Surface tension	$N\ m^{-1}$
η_{e^-}	Ohmic loss from electron transport	V
η_{H^+}	Ohmic loss from proton transport	V
η_{HOR}	Kinetic loss from the hydrogen oxidation reaction	V
η_{OCV}	Open circuit voltage loss	V
η_{ORR}	Kinetic loss from the oxygen reduction reaction	V
η_{mx}	Mass-transport loss	V
η_{th}	Thermodynamic efficiency	
κ	Thermal conductivity	$W\ m^{-1}\ K^{-1}$
σ	Scaling factor	
τ	Tortuosity	
υ	Volume fraction	

Roman symbols

Symbol	Description	Unit
a	Ion beam radius	m
C	Concentration	$mol\ m^{-3}$
d	Mean pore diameter	m
E^{O}_{Cell}	Standard cell potential	V

E^{O}_{anode}	Standard potential at anode	V
$E^{O}_{Cathode}$	Standard potential at cathode	V
D	Local diffusion coefficient	$m^2 s^{-1}$
D^{eff}	Effective diffusion coefficient	$m^2 s^{-1}$
D^{b}	Bulk diffusion	$m^2 s^{-1}$
D^{K}	Knudsen diffusion coefficient	$m^2\ s^{-1}$
f	Stretching factor	
Δg	Change in Gibbs free energy	$J\ mol^{-1}$
Δh	Change in enthalpy	$J\ mol^{-1}$
$i\ (subscript)$	Diffusing species	
j	Diffusion flux	$mol\ m^{-2} s^{-1}$
K	Thermal conductivity	$W\ m^{-1} K^{-1}$
K^{eff}	Effective thermal conductivity	$W\ m^{-1} K^{-1}$
L_c	Shortest convoluted path length	m
L	Euclidean distance	m
M	Molar mass	$kg\ mol^{-1}$
P	Beam power	W
p_{eq}	Equilibrium pressure	Pa
$P\ (subscript)$	CB or CG/FG particle	
$\dot{Q}$	Heat flux	$W\ m^{-2}$
R	Universal gas constant	$kg\ m^2\ s^{-2}\ K^{-1}\ mol^{-1}$
T	Temperature	K
V	Cell potential	V

Chapter 1.

Introduction

A fuel cell is an electrochemical device that converts the chemical energy stored in the fuel and the oxidant into electricity. A fuel cell differs from a battery with regards to storage of the reactants external to the cell instead of internal storage. This leads to continuous operation of the fuel cell if a supply of fuel and oxidant is available. There are varieties of fuel cell designs based on ion transport medium (electrolyte), operating temperature, fuel type, and power output. The polymer electrolyte membrane (PEM) fuel cell may become the prominent energy delivery device of the 21st century. The characteristics of the PEM fuel cell are low operating temperature (60ºC – 80ºC), high power density, and low emission. The PEM fuel cell can be used as a power generator or an engine for a wide range of motive, stationary, and portable applications.

1.1. Working principle

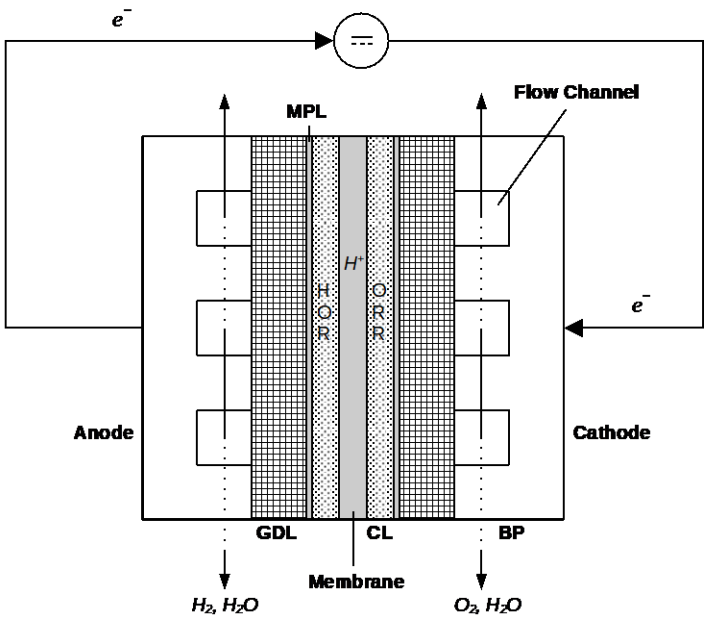

Figure 1.1. Schematic of a single cell PEM fuel cell.

A PEM fuel cell is composed of an anode electrode, the electrolyte membrane, a cathode electrode, and bipolar plates (BPs) (Figure 1.1). The porous anode and cathode electrodes consist of the gas diffusion layer (GDL), the catalyst layer (CL), and often a microporous layer (MPL) between the GDL substrate and the CL. The porous CL consists of many agglomerates, each of which is made up of a cluster of carbon black particles with dispersed platinum catalyst particles on its surface. The platinum-carbon catalyst particles are held together by an ionomer. In the PEM fuel cell, hydrogen supplies fuel to the anode electrode. The hydrogen diffuses through the anode GDL and the anode MPL before reaching the anode catalyst layer (ACL). The hydrogen at the ACL is oxidized via the hydrogen oxidation reaction (HOR):

$$H_2 \rightarrow 2H^+ + 2e^- \qquad E^O_{anode} = 0.0V \tag{1.1}$$

The protons travel through the ionomer in the ACL and the membrane electrolyte layer to the cathode catalyst layer (CCL). Meanwhile, electrons travel via the electron conducting particles (catalyst and carbon black) in the ACL to the anode GDL, and then via the anode BP to the external circuit, doing the electrical work before arriving at the cathode. Then electrons are transported through the cathode BP to cathode GDL and finally reaches the CCL. At the same time, oxygen or air is supplied to the cathode electrode. The oxygen diffuses through the cathode GDL and the cathode MPL before reaching the CCL. The oxygen at the CCL is reduced via the following oxygen reduction reaction (ORR):

$$2H^+ + 2e^- + \frac{1}{2}O_2 \rightarrow H_2O \qquad E^O_{cathode} = 1.23V \tag{1.2}$$

Although the half-cell reactions, equations *1.1* and *1.2* are written as a single step, multiple intermediate reaction pathways are possible at each of the electrodes.

The overall reaction is the fuel (hydrogen) reacting with the oxidant (oxygen) producing water, electrical energy, and waste heat:

$$H_2 + \frac{1}{2}O_2 \rightarrow H_2O + electrical\ energy + heat \qquad E^O_{cell} = 1.23V \tag{1.3}$$

The product water formed in the catalyst agglomerate reaches the pore space in the CCL where it is desorbed into either water vapour or liquid water depending on the local relative humidity. The water is then transported through the cathode GDL and removed from the cell via the oxygen or air stream in the cathode flow channels. However, part of the product

water may also travel through the membrane and reach the anode ionomer. This occurs because of the gradients of hydraulic pressure and/or water concentration between the CCL and the ACL. The back diffused water (phenomenon referred to as “back-diffusion”) is then transported via the pore space in the ACL where it is desorbed into either water vapour or liquid water depending on the local relative humidity. The back diffused water is then transported through the anode GDL and removed from the cell via a hydrogen stream in the anode flow channels. The phase change of water within the fuel cell is dictated by local heat generation or cooling since the local relative humidity (RH) is strongly linked to the local temperature. The presence of MPL between GDL and CL is known to assist water transport and removal processes, although the exact mechanisms are still debated [1]. Waste heat is generated due to the irreversibility of converting chemical energy into electrical energy. Also, the continuous transport of electrons and protons through the different layers of the fuel cell results in waste heat generation. The primary mode of heat transfer within the fuel cell is via heat conduction through the solid phase and to a lesser degree via convection or radiation in the pore phase. Therefore, estimating the effective thermal conductivity of individual layers is necessary to determine the heat transfer within the fuel cell. The reactant gas stream in the anode and cathode flow channels eventually removes the heat generated within the fuel cell components. In addition, a cooling flow channel built within the bipolar plate can remove the heat generated, especially for a higher power output fuel cell stack.

The fuel cell thermodynamic efficiency is given by the ratio of the actual electrical work to maximum available work:

$$\eta_{th} = \frac{actual\ electrical\ work}{maximum\ available\ work} = \frac{\Delta g}{\Delta h} \qquad 1.4$$

where $\Delta g\ (J\ mol^{-1})$ is the change of Gibbs free energy per mole of hydrogen for the overall reaction and $\Delta h\ (J\ mol^{-1})$ is the change in enthalpy per mole of hydrogen for the overall reaction [2]. By using equation *1.4*, the maximum theoretical efficiency can be calculated to be 83% for liquid water as the by-product at 25ºC. The equation *1.4* cannot, however, determine the electrical energy output for a specific fuel cell configuration.

1.2. Polarization curve

During the fuel cell operation, multiple complex interlinked phenomena occur. These phenomena influence reaction pathways, reaction kinetics, mass and species transport, and energy losses. An understanding of electrochemical kinetics is necessary to assess the impact of the individual fuel cell component's design on overall system performance. A graph of voltage versus current is used to describe fuel cell performance, usually referred to as a polarization curve. Three regions (voltage losses) that characterize the polarization curve are kinetic losses, ohmic losses, and mass-transport loss (Figure 1.2).

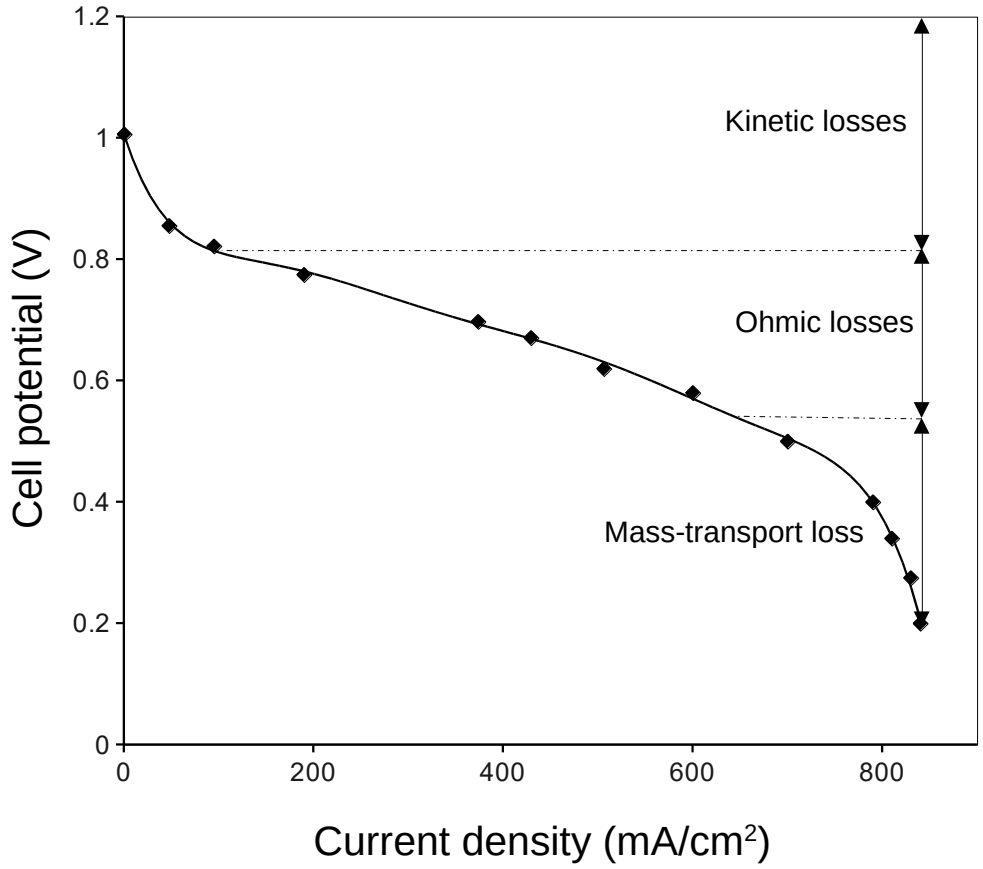

Figure 1.2. Sample fuel cell polarization curve showing kinetic losses, ohmic losses, and mass-transport loss.

Kinetic losses are related to processes occurring during electrochemical reactions on the electrode surfaces (HOR or ORR). They are dominant under low power density operations and can be minimized by using a catalyst. In PEM fuel cells, the platinum catalyst is used to speed up reaction rates. The cell voltage at zero current is referred to

as open circuit voltage (OCV). It is always lower than the reversible voltage (1.23 V, equation *1.3*) due to fuel crossover and internal currents. The ion conducting membrane is electrically nonconductive and ideally impermeable to gases. In practice some amount of hydrogen from the anode travels through the membrane and reacts with oxygen at the cathode resulting in fewer electrons traveling through the external circuit, thus reducing the overall efficiency of the fuel cell. The ohmic losses are associated with electronic and protonic resistances. The electronic resistance arises due to electrons' mobility through various diffusion layers and interconnections between layers. The transport of ions (H^+) through the PEM and ionomer in the CLs corresponds to protonic resistance. Protonic resistance is inversely proportional to the relative humidity of the cathode electrode [3] and is only a weak function of temperature [4].

Mass-transport loss arises due to a decrease in the concentration of reactants at reaction sites, as they are consumed along the flow channel from the inlet to the outlet. At higher current density there is a sharp drop in voltage due to an insufficient supply of reactant to the reaction sites. Even with a sufficient supply of reactant sometimes excess water accumulates blocking reaction sites and resulting in a mass-transport loss (commonly referred to as 'water flooding' phenomena). Therefore, the removal of excess water from the electrodes is necessary for operating the PEM fuel cell at a high current density. The relationship between operating cell potential, reversible potential, and voltage losses is:

$$V = \eta_{OCV} - \eta_{HOR} - \eta_{ORR} - \eta_{e^-} - \eta_{H^+} - \eta_{mx} \qquad 1.5$$

where η_{OCV} is the OCV loss, η_{HOR} is the kinetic loss from the HOR, η_{ORR} is the kinetic loss from the ORR, η_{e^-} is the ohmic loss from electron transport, η_{H^+} is the ohmic loss from proton transport and η_{mx} is the mass-transport loss.

During the last decade, significant progress has been made in increasing PEM fuel cell performance and durability. The performance and durability of the PEM fuel cell is strongly linked to the materials used in the fuel cell system, notably the proton exchange membrane, catalyst layers, and gas diffusion layers of the membrane electrode assembly (MEA) [5]. The morphological characterization and thorough knowledge of the properties of these materials are necessary for the design optimization of electrode materials. Numerous experimental and numerical studies have been published to describe transport

phenomena at micro/nano length scales in the PEM fuel cell and their impact on fuel cell performance. These studies inherently make use of key parameters such as porosity, mean pore diameter, diffusivity, tortuosity, thermal conductivity, electrical conductivity, and permeability which depend on the detailed morphology of the material [6–8]. It is nearly impossible to rigorously determine such parameters without access to accurate three dimensional (3-D) structural information.

1.3. The gas diffusion layer

The catalyst coated membrane (CCM) found at the center of the PEM fuel cell is made up of the membrane (10 - 50 μm) coated with the platinum catalyst layer (10 – 20 μm) on either side. Surrounding this, 150 – 400 μm thick GDLs connect the CCM to the BPs at the anode and cathode electrodes. The BPs have flow channels for distributing fuel and oxidant over the surface of the electrodes. The GDL acts as the transitional material between CCM and BP and has several functions:

- The GDL is sufficiently porous (≥75%) to allow for free diffusion of reactant gases from the flow channel to the reaction sites, including reaction sites located under both channels and lands of the BP.
- The solid phase of the GDL provides mechanical stability for the MEA and a pathway for thermal and electrical conduction between the CL and BP.
- The GDL serves in the removal of product water at the cathode CL reaction sites to reach the flow channels without affecting the flow of reactants.
- The GDL maintains good contact with the BP and CL to minimize thermal and electrical contact resistance.

Carbon papers, felts, and cloths are commonly used as GDL substrates, consisting of a matrix of carbon fibers (approximately 8 μm diameter) held together by a graphitized binder [9]. The fibrous substrate acts as backing material which governs the GDLs mechanical behavior under compression, bending and shear strength. GDL consists of macro-scale pores ranging from 10 μm to 100 μm. The hydrophobic agent namely the polytetrafluoroethylene (PTFE) is added to the GDL substrate to aid with liquid water removal.

The optimal GDL substrate design is essential to avoid ‘water flooding’ phenomena and to operate the cell at high power density [10]. Therefore, a great deal of research has

been dedicated to the estimation of the transport properties of the GDL by theoretical and analytical methods, and the obtained mathematical expressions are commonly employed in the macroscopic PEM fuel cell modelling and analysis [11]. These formulations assume that the porous media consists of a uniform, repetitive solid matrix, which is a significant simplification in the case of the GDL. Consequently, the resulting estimations of transport properties and fuel cell performance have a high degree of uncertainty [12]. Analytical studies are often complemented by experimental work, both *ex situ* and *in situ* techniques are employed in determining the transport properties [13–19]. For instance, diffusion coefficients have been measured using both *ex situ* and *in situ* methods for different GDL materials [13,14,18]. Numerical methods are also becoming more popular, such as the stochastic virtual modelling technique proposed by Schladitz *et al.* [20–22]. The stochastic technique is used to generate 3-D structures based on known parameters as inputs, *e.g.,* porosity, fiber diameter, and section intensities, which can be measured either by experiment or 2-D image analysis of material samples [23,24]. The obtained 3-D structural model is then used as the domain for numerical simulations of transport properties [25,26]. A useful summary of this approach is provided in the book chapter by Mukherjee *et al.* [27].

1.3.1. The microporous layer

The microporous layer (MPL) is a relatively recent addition to the GDL that is arguably the least studied layer in the MEA with regards to its properties and role towards performance enhancement [11]. The MPL generally consists of a mixture of carbon black nanoparticles and PTFE, and is coated on the GDL side facing the CL. The carbon nanoparticle based MPL has a mean pore size in the range 15 – 200 nm, along with surface cracks ranging from 5 to 25 μm [28,29]. MPL enhances the structural integrity of the MEA by creating a buffer region between the GDL and CL. MPL effectively protects the CCM against perforation by the GDLs carbon fibers. There is a clear consensus that MPL has a positive impact on overall fuel cell performance [1,30]. However, there is a lack of understanding of the underlying mechanisms that create the positive effect [31,32]. The MPL requirements that guide the design process are:

- Water transport properties that strike a balance between water removal and water supply;

- Gas permeability that provides a sufficient supply of reactants to the catalytic sites;
- Excellent electrical conductivity and low interfacial electrical contact resistance;
- Thermal conductivity that promotes temperature uniformity, balanced thermal management, and low interfacial thermal contact resistance;
- High structural integrity and optimal pore size (micropores and mesopores) distribution;
- Enhanced chemical stability under different operating conditions; and
- Low cost manufacturing.

The accurate determination of MPL transport properties is critical for further advances in this area. Provided that MPLs of realistic thicknesses cannot be fabricated as discrete objects, direct measurements of their transport properties are usually not feasible. Instead, MPL transport properties are estimated by comparing the measurements on bare GDL and GDL-MPL assembly. This approach was used to estimate the diffusion coefficient of commercially available carbon felt (SGL®) and found a 39% reduction in through-plane diffusivity upon application of MPL onto the GDL surface [19]. Numerical studies based on stochastic models have also reported that the presence of MPL leads to reduced diffusivity of the GDL-MPL assembly [33,34]. Experimentally obtained values of MPL thermal conductivity cover a wide range (0.035 - 3.87 W m^{-1} K^{-1}) [35–41]. The structural properties of the MPL, including penetration depth, thickness, and porosity, are normally estimated using crude methods based on visual inspection or capillary pressure measurements [42,43]. The MPL specific properties estimated from composite GDL substrates coated with MPL have a high degree of uncertainty.

1.4. Imaging techniques

The morphological characterization of the PEM fuel cell electrodes is possible at various length scales ranging from micro to nanometers (Figure 1.3). The mercury intrusion porosimetry (MIP) and gas adsorption techniques can be used to estimate bulk porosity, pore sizes, and surface area [44,45]. The MIP is a destructive technique but an easy method to characterize porous media that contain pores in the range 0.003 μm to 360 μm [46]. The mercury's distinctive high surface tension makes the method appropriate to characterize porous media that contain both hydrophobic and hydrophilic pores. The

correlation between applied pressure and injected mercury into the sample is used to determine pore size distribution. Both MIP and gas adsorption techniques are limited by the effect of pore throats [44] and inaccessible closed pores [47]. The experimental methods that measure bulk properties are unsuitable for detailed characterization of the internal structure. Since the PEM fuel cell materials are inherently heterogeneous, rigorous quantification of the properties in multiple directions and locations is imperative. The use of morphological characterization of materials is further augmented by the fact that a small variation in manufacturing can lead to substantial changes in bulk properties. Therefore, the establishment of a microstructural analysis tool is necessary to accurately capture the unique internal structure and thereby estimate consistent transport properties.

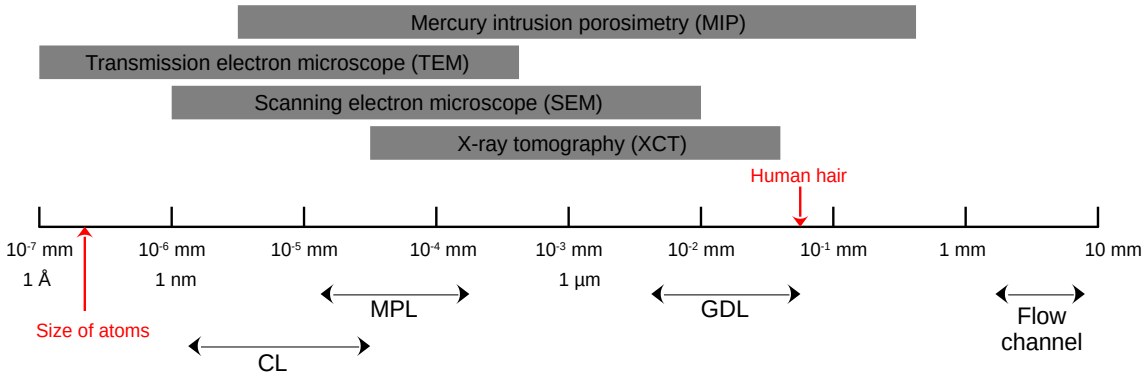

Figure 1.3. Resolution of various morphological characterization techniques (MIP, TEM, SEM, and XCT) and mean pore size range in CL, MPL, and GDL.

The use of imaging techniques can provide local information in multiple directions usually at the cost of a smaller region of interest (RoI). The commonly used tomography methods to obtain the detailed internal structure of the fuel cell electrodes are X-ray computed tomography (XCT), transmission electron microscopy (TEM), and focused ion beam-scanning electron microscopy (FIB-SEM). The TEM in conjunction with the ultramicrotome can be used to obtain volumetric structural information [48]. The superior resolution capability of TEM makes it possible to resolve the dispersed platinum catalyst particles on carbon support as well as ~10 nm thick ionomer around the carbon support [49]. The ultramicrotome based sample preparation is shown to be less damaging to the CL structure when compared to FIB [49]. However, the size of the representative volume that can be analyzed is a limiting factor to fully characterize the morphology of the structure [50,51].

The XCT is a proven, non-destructive method to resolve the 3-D structure of porous materials with high spatial resolution. Advanced X-ray synchrotron facilities can provide a resolution up to 50 nm [52], a level which has also been achieved using commercial XCT equipment with specialized X-ray optics [53]. The low energy (5.4 keV) nano-XCT has been shown to improve the contrast among materials with low density and low atomic number [54]. The differentiation of carbon black and PTFE within MPL has been achieved by manually selecting the greyscale value threshold and pre-knowledge of carbon black and PTFE weight fractions[55]. However, the soft nature of the MPL poses a technical challenge (in terms of time, cost, and specialized equipment) to prepare thin samples suitable for nano-XCT.

SEM is a well known technique that provides high contrast and high-resolution images. However, SEM is limited to two-dimensional (2-D) imaging and image segmentation can be harder due to the “strong edge” effect (the interfacial edge between the solid and pore phase is clearly visible). Alternatively, a dual beam FIB-SEM system can be used to obtain three-dimensional (3-D) visualization of the material. In FIB-SEM, an ion beam is used to erode the material (sectioning) and the SEM is used to image the exposed material. A stack of 2-D images through the thickness of the material is obtained by repeating the sectioning and the imaging procedure [56]. The use of epoxy resin to fill the pores in the positive electrode of lithium ion battery [57] and the anode of solid oxide fuel cells (SOFC) [58] has been shown to alleviate the “strong edge” effect, improving accuracy and reducing segmentation time. The use of epoxy resin or other high contrast material in CL and MPL is problematic since only connected pores can be filled and the epoxy resin can also cause damage to the delicate structure of CL and MPL.

1.5. Scope and objectives

The objective of the present work is to develop an enhanced morphological characterization framework specifically for the MPL, featuring a customized FIB-SEM imaging method that does not require any sample preparation and accurately reproduces the true original structure. Two types of MPL materials are characterized: the carbon black (CB) nanoparticle and the graphite particle based MPLs. In contrast to previous studies [59–61], both the directional and spatial heterogeneity of the sample is considered. In addition, the effects of FIB sectioning step size and direction are analyzed to quantify any deposition or damage caused by the ion beam and to decouple the impact of the milling

on the results. Finally, new procedures for extraction of structural parameters and effective properties are presented, including porosity, pore size distribution, effective diffusivity based on combined bulk and Knudsen diffusion, tortuosity, and effective thermal conductivity. The proposed characterization framework is validated with the measured pore size distribution of a physical MPL material coated on a blank substrate, and the results are compared to measured GDL properties and literature data.

1.6. Thesis structure and contributions

The organisation of this thesis is as follows:

- In Chapter 2, the customized framework is set up to obtain the 3-D morphological characterization of the MPL materials. The FIB-SEM imaging technique procedure is established to capture high resolution images of the CB and graphite particle based MPLs. The specific image processing protocols are set up to capture the internal microstructure of the MPL. Details are given for the novel algorithm used to obtain the structural parameters and transport properties of the reconstructed models of the MPL.

- In Chapter 3, the 3-D reconstructed MPL models are used as computational domains to deduce key structural parameters and effective transport properties. The results obtained are validated against the experimentally measured pore size distribution and porosity. Wherever possible the calculated effective transport properties of the MPL samples are compared to measured GDL properties and other relevant data from the literature.

- In Chapter 4, the key findings, and observations of the 3-D framework for characterizing the MPL materials are listed. The differences between the two types of MPL materials studied are summarized. Also, potential future work that can be carried out is suggested.

The publications arising from this work are:

- “A Customized Framework for 3-D Morphological Characterization of Microporous Layers” **Nanjundappa, A.,** *et al.,* Electrochimica Acta 110 (2013), 349-357, 2013

- “Three-Dimensional Morphological Characterization of Micro Porous Layers” Sadeghi Alavijeh, A., **Nanjundappa, A.,** *et al.,* 222nd ECS Meeting, Honolulu, 2012

- “Characterization of Micro-Porous Layer: Experimental Images to Multiscale Multiphysics Modelling” **Nanjundappa, A.,** *et al.,* 63rd Annual Meeting ISE, Aug 2012, Prague, 2012

Chapter 2.

Methodology

The word tomography is derived from the Greek words, ‘tomos’ (slice or section) and ‘graphein’ (to write or to describe). The FIB-SEM nanotomography exemplifies this etymology. The FIB microscopy is like SEM, except that the beam that is rastered over the sample is an ion beam instead of an electron beam. In the FIB-SEM dual beam system, the sample is sectioned using the FIB and the result is written in the form of digital data via an SEM scan. A 3-D structure of the sample is obtained when the individual sections (tomograms) are stitched together representing the original object. The factors that influence the results when performing 3-D reconstruction of materials by serial sectioning are:

- The size of the feature being reconstructed when compared to instrument resolution;
- Ion beam damage and heating;
- Data collection: maintaining parallel slices, the precision of slicing increment and planarization of the surface; and
- 3-D reconstruction: image processing routine (complexity vs. accuracy), data-set size and quantitative data analysis.

Part of the material in this chapter is excerpted, changed, and reproduced with permission from the following paper that I co-authored:

“A Customized Framework for 3-D Morphological Characterization of Microporous Layers” Nanjundappa, A., et al., Electrochimica Acta 110 (2013), 349-357, 2013.

2.1. Image acquisition

The FEI Dual Beam (DB) Strata® 235 FIB-SEM system was used to perform nanotomography for the following three MPL samples: (1) Carbon black (CB) nanoparticle MPL with 40% PTFE; (2) Coarse graphite (CG) particle MPL with 18% PTFE; and (3) Fine graphite (FG) particle MPL with 18% PTFE (Figure 2.1). The high precision Ga^+ ion milling enables serial cross-sectioning of the surface. Combining ion milling with high resolution

cross-sectional SEM imaging results in high-quality volumetric information of the material. The two beams have a coincident angle of 52°, as shown schematically in Figure 2.2. Because of the delicate nature of the MPL structure, the present imaging method was developed intentionally to avoid sample preparation that may otherwise damage the structure. The image acquisition process involves the following steps: (1) deposition of platinum layer; (2) milling a promontory; (3) fiducial mark; (4) milling; and (5) imaging.

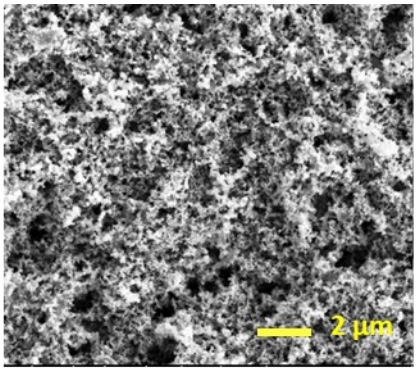

(a) Carbon black nanoparticle

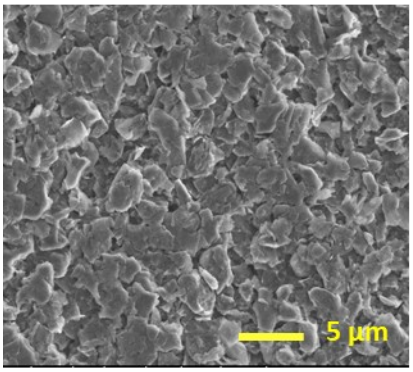

(b) Fine graphite particle

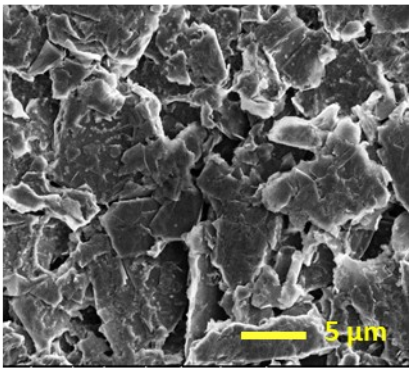

(c) Coarse graphite particle

Figure 2.1. Top-down SEM images of the three MPL samples under study: (a) Carbon black nanoparticle; (b) Fine graphite particle; and (c) Coarse graphite particle.

The surface of the sample was coated with a thin layer (100 – 200 nm) of platinum (Pt) prior to side-wall milling to prevent damage to the delicate structure of the MPL from Ga^+ ion bombardment. The Pt layer also reduces the redeposition effect caused by ion beam induced decomposition of the precursor gases. Further, the Pt layer serves to planar the surface which would prevent striations in the face of the cross section (the “curtain effect”) and avoid the swelling effect [56]. The cross-sectional surface of the specimen to be imaged was exposed as a promontory by milling away the surrounding region, rather

than using a large rectangular trench [58,59]. The promontory (Figure 2.2) compared to a rectangular trench reduced horizontal gradients and shadowing artifacts, both of which would otherwise complicate the image processing. The fiducial mark is the reference mark that is visible in all the 2-D SEM images. The fiducial mark is necessary for aligning the stack of 2-D images. Here the fiducial mark was created by sputtering a “rectangular pillar” like shape far from the cross-sectional surface to be imaged.

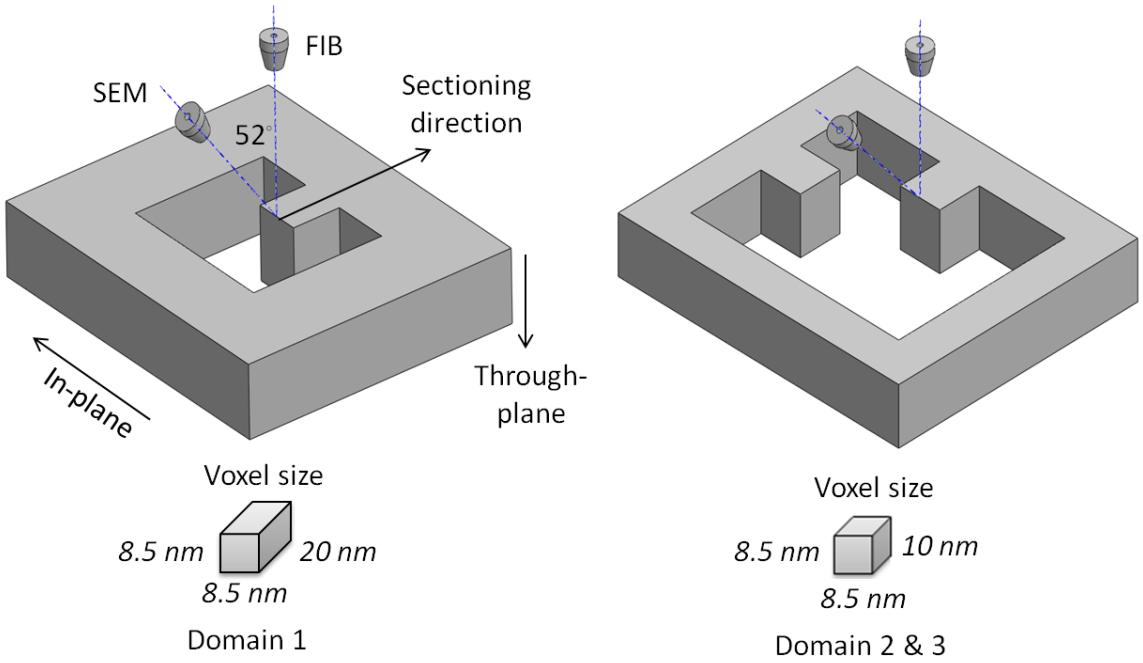

Figure 2.2. Schematic of the FIB-SEM imaging configuration. The sectioning step sizes were 20 nm for carbon black nanoparticle MPL Domain 1 and 10 nm for Domains 2 and 3. The sectioning directions for Domains 2 and 3 were mutually perpendicular to each other.

The primary concern in FIB milling of MPL samples is that the Ga^+ ion beam can cause local heating, damaging the structure and changing the chemical structure. The heat damage depends on the following factors: (1) ion beam current and radius; (2) accelerating voltage of ion beam; (3) thermal conductivity of the sample; (4) sample geometry; and (5) contact to a heat reservoir. The ion beam’s kinetic energy is converted to heat, with only a small fraction emitted as energetic particles or radiation. The steady-state temperature rise of the sample can be determined by the following equation [62]:

$$T = \frac{P}{\pi a \kappa} \qquad 2.1$$

where P is the beam power, *a* is the radius of the circular ion beam profile on the sample surface and κ is the thermal conductivity of the sample. For commercially available FIBs the ratio "P/a" ranges from 1 $W\,m^{-1}$ to 1000 $W\,m^{-1}$. The temperature rise is negligible for samples with good thermal conductivity even for extreme beam conditions. For carbon black nanoparticle MPL ($\kappa \sim 0.1\,W\,m^{-1}\,K^{-1}$), temperature rise of less than 10º C can be achieved with "P/a" values of less than 3 $W\,m^{-1}$, which is at the low end of what is available in commercial FIBs. Ion beam heating effects can also be diminished by placing the sample in contact with a heat reservoir.

The highest ion beam accelerating voltage available in FEI DB Strata® 235 is 30 kV. The ion beam diameter decreases with an increase in ion beam voltage. The highest resolution ion beam image is possible with the smallest ion beam diameter. There are four default low ion beam currents available with the FEI DB Strata® 235: 1 pA, 10 pA, 30 pA, and 50 pA. 1 pA and 10 pA ion beam currents are not suitable for milling the CB MPL due to difficulty in obtaining a clear focused image. The 30 pA ion beam current was chosen over 50 pA to reduce re-deposition effects and obtain clear, focused images. Thus, an optimized milling current of 30 pA at 30 kV accelerating voltage was determined to prevent Ga^+ ion deposition and damage of the bare specimen. The selected milling current is much lower than that used in previous studies [60,61] and is required to obtain a realistic structural reconstruction without additional sample preparation.

To reduce the time and cost of experimentation compared to complete statistical analyses [60,63], a manual screening approach was used to identify a suitable region of interest that is representative of the overall structure of the sample. Three different imaging domains of the CB MPL were selected for this study, as illustrated in Figure 2.2. The domains were chosen to analyze the effect of sectioning step size and direction. For Domain 1, a step size of 20 nm was used. In addition, two more adjacent domains (Domains 2 and 3) were selected with a lower step size (10 nm) and mutually perpendicular sectioning directions to account for directional heterogeneity as well as spatial heterogeneity of the structure (Figure 2.2). For Domain 1, 70 slices were milled while for Domains 2 and 3, 140 slices were milled. For each of the three domains, high-resolution SEM images of the slices with 8.5 nm pixel size were captured. In theory, there is no limit to the number of slices that can be obtained, but in practice, the limitations are enforced by time constraints. The total image acquisition time for Domain 1 was about 10

hours and for Domain 2 and 3 about 16 hours. A raw image of a CB MPL slice is shown on the left in Figure 2.3, revealing round carbon nanoparticles held together by the PTFE.

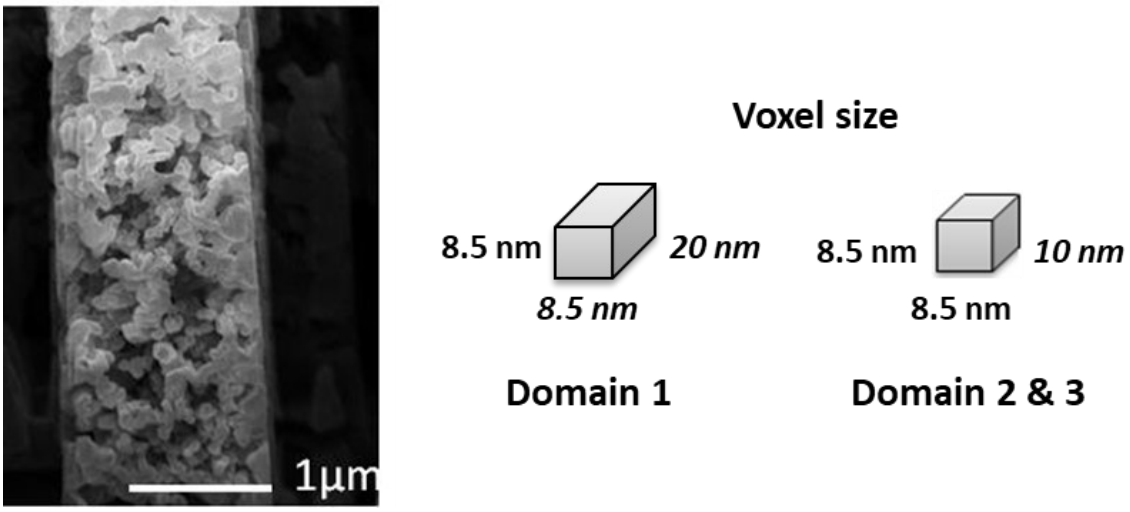

Figure 2.3. Raw SEM image of carbon black nanoparticle MPL and voxel size for Domains 1, 2, and 3.

To reduce the cost and time for image acquisition the proper ion beam milling current for the FG and CG MPL samples was determined to be 50 pA and 100 pA respectively. The higher beam currents for FG and CG MPL samples result in faster mill rate and tend to increase the amount of re-deposited material and/or melt the surrounding material. The systematic study showed the ion beam heating damage in polymers (some properties analogues to MPL) can be avoided by maintaining a low ion beam current, less than 100 pA [64]. For ion beam currents under 100 pA, the polymer sheet kept its nanostructured morphology and wrinkle free on the sheet surface [64]. The inherent thermal conductivity of graphite particle is orders of magnitude higher compared to the CB nanoparticle; therefore, the temperature rise for the FG and CG samples (equation *2.1*) under higher beam current is lower than that of CB MPL sample. Based on the features to capture and the total milling time, the right step size for FG and CG MPL samples were 50 nm and 100 nm respectively. For the FG MPL sample, 80 slices were milled while for the CG MPL sample, 40 slices were milled. Only one domain was obtained for both FG and CG samples with the SEM image resolution of 25 nm and 37 nm respectively. Raw images of FG and CG MPL slices are shown in Figure 2.4, revealing the graphite particle's disc-like shape along its thickness. Table 2.1 summarize the SEM image resolution, FIB step size and domain size for three MPL samples.

Table 2.1 Image resolution, step size and domain size for three MPL samples

Sample		SEM Image resolution (nm)	FIB Step size (nm)	Domain size (TP * IP * SD) µm
CB	Domain 1	8.5	20	2.8 * 1.4 * 1.4
	Domain 2	8.5	10	2.8 * 1.4* 1.4
	Domain 3	8.5	10	2.8 * 1.4 * 1.4
FG		25	50	7 * 5 * 4
CG		37	100	10 * 10 * 4

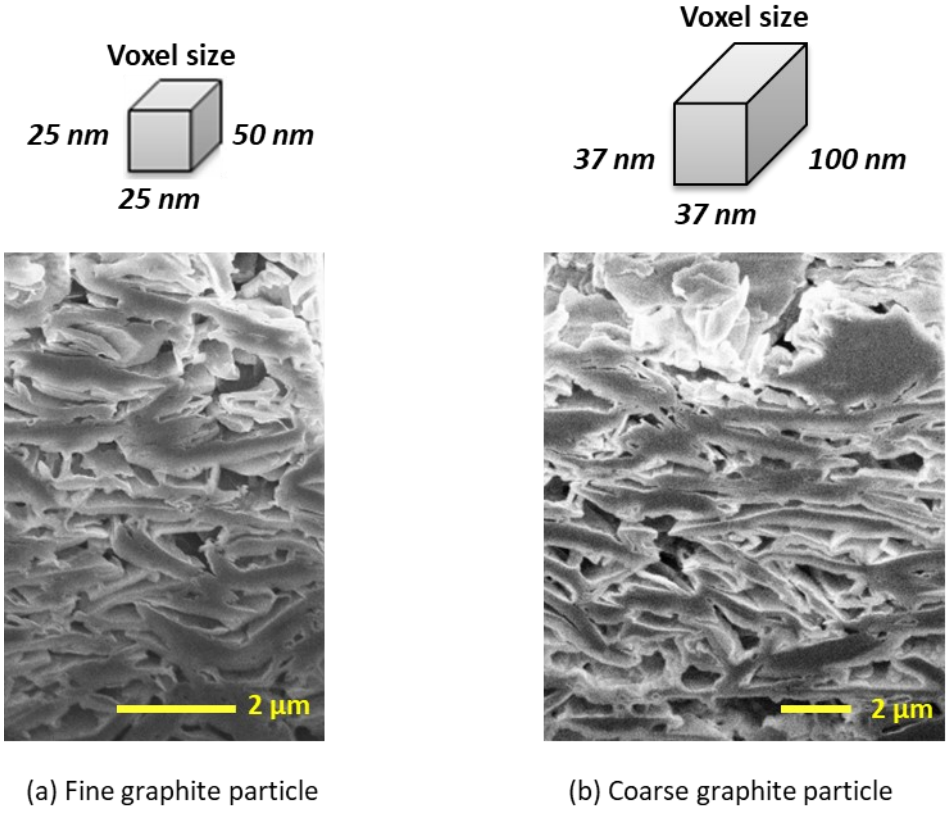

Figure 2.4. Raw SEM image and voxel size of the a) fine graphite particle and b) coarse graphite particle MPLs.

2.2. Image processing[1]

The FIB-SEM raw images need to be processed to ensure accurate quantification of the internal structure of the sample. MPL specific image processing protocols were established in the present study using ImageJ® open source scientific image analysis software. The main steps in the image processing are (1) image alignment; (2) viewing angle correction; (3) cropping; (4) image noise reduction; and (5) segmentation, as depicted for the CB MPL image in Figure 2.5. Ultra high resolution SEM images are needed to resolve the nanoscale features of the MPL. A slight change in the viewing angle will result in beam shift and image displacement in successive slices. Misalignment was addressed by using an image alignment algorithm, the Lucas-Kanade algorithm [65]. The fiducial marker present in all the image slices (shown on the left side of the raw image in Figure 2.5) acts as a matching feature to make the alignment process straightforward. The lateral dimensions along the x-axis were obtained by the calibrated SEM sliced image. Next, the off-normal viewing angle θ, equal to 52° between the SEM beam source and the cross-sectional surface being imaged was considered. The viewing angle correction was implemented by stretching the images vertically along the y-axis, by the factor f, accounting for angular projection:

$$f = \frac{1}{sin(\theta)} \tag{2.2}$$

Once all the SEM images were properly aligned and viewing angle correction applied, the final domain (RoI) was cropped. It is necessary to convert the individual 2-D pixel into a corresponding voxel (3-D pixel) for further evaluation of structural properties. The image stack is stretched and interpolated in the sectioning direction to obtain the voxels. The voxel is defined by x, y, and z position in the volume as well as by the vector s, the secondary electron signal information. The next step is to develop proper segmentation protocols to transform each voxel in the entire grayscale image into a binary dataset consisting of pore and solid phases. The bright areas in the SEM image correspond to the solid phase cut by the FIB, and the dark areas are the pore phase. The solid phase of the MPL material includes hydrophilic carbon nanoparticles and

[1] The rest of the chapter describes the image processing steps and determination of structural properties using the CB MPL datasets as an example. The process is also applicable to FG and CG MPL datasets.

hydrophobic PTFE. These two solid phases were difficult to distinguish in the obtained FIB-SEM datasets and beyond the scope of the present study. Despite taking advantage of cross-sectioning a promontory, the raw images inevitably have horizontal gradients and shadowing artifacts. These artifacts reduce the accuracy of the image segmentation into solid and pore phase. The artifacts were corrected by applying median filter as a preconditioning step before the segmentation. The absence of brightness gradients between consecutive images was verified and adjusted using a brightness and contrast (B&C) tool for each image slice.

Image segmentation is an active field of research, and there are three segmentation methods: manual; auto; and semi-auto methods. The simplest and most precise method of segmentation is manual segmentation; however, the method is time consuming, can be subjective and is impractical for large datasets. The most commonly employed method to segment voxel/pixel based datasets is auto segmentation, where a certain value threshold is set to automatically binarize the image [66]. This helps to finish the segmentation quickly, but the accuracy is lower than that of manual segmentation. If brightness intensity is the only criteria used to set the threshold value, then applying auto segmentation tends to falsely assign the voxels as pores instead of solids or vice-versa. The semi-auto approach consists of two steps: first, the optimized threshold value is applied during the pre-selection stage and then the results are improved manually during the second stage [67]. This semi-auto approach reduces the segmentation time compared to the manual segmentation, but it is still time intensive due to the manual screening after the auto segmentation.

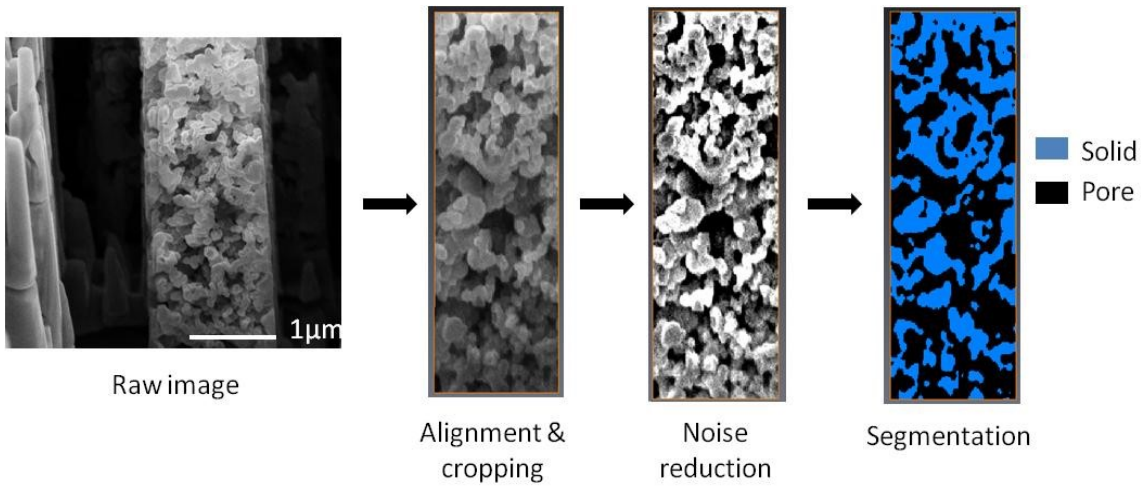

Figure 2.5. The main image processing steps.

In a SEM image, the interfacial edge between the solid and pore phase is clearly visible. The downside of this “strong edge” effect of a SEM image is that the interfacial edge that encapsulates the solid phase is brighter than the inside part of the material. When imaging a highly porous MPL microstructure the large focal depth in a SEM image results in material from the layers beneath to be visible through the pores (“shine-through” artifact). Hence, there are two problems in applying the certain value thresholding algorithm. Firstly, the solid phase is reconstructed as a hollow structure and secondly, the solid phase is captured even before appearing in the cross section, resulting in a pillar like structure along the sectioning direction. The widely used automatic global thresholding methods applied to the MPL structural characterisation are Otsu’s and ISODATA [55,59,60,63,68]. The inaccuracies in the estimated material properties due to the application of automatic thresholding method has been demonstrated quantitatively with tortuosity values [68] and pore-volume [54]. In the current study keeping accuracy in mind, manual segmentation is employed to circumvent the “strong edge” effect and “shine-through” artifact. The manual segmentation process consists of tracking the changes between two consecutive images to differentiate the solid phase from the pore phase. Further the process consists of finding the solid phase contours using the brightness gradient within each image. Finally, the obtained segmented 3-D domain accurately depicts the internal structure of the MPL.

2.3. Calculation of porosity and pore size distribution

The pore size distribution (PSD) is a key characteristic of GDL and MPL materials. However, to the author’s knowledge, the explicit pore size distribution of pure MPL materials is unknown and has not been previously reported in the literature. The present method employed to calculate the pore sizes of the 3-D reconstructed MPL structure is based on the Euclidean distance transform (EDT) [69]. For a given binary image (zeros and ones), as illustrated in Figure 2.6a, the Euclidean distance is calculated from each voxel (pixel in the 2-D example) with value 1 to the nearest voxel with value 0. This results in a distance map, where every voxel representing pore phase is assigned the Euclidean distance to the nearest voxel representing solid phase. The pores are then defined as spheres with a center given by the maxima of the distance map and the height of the maxima corresponding to the sphere (pore) radius. The EDT algorithm for a 2-D circular hole is depicted in Figure 2.6b as an example of the results obtained by the algorithm. The

3-D EDT used to calculate the PSD in the present work was implemented using the MATLAB® function “dwdistsc1” [70]. The function “dwdistsc1” is based on a fast line algorithm and implemented in a vector processing architecture. It can handle large datasets and is faster than the native MATLAB® function “bwdist”. Further, the function “dwdistsc1” can handle anisotropic aspect ratio voxel datasets, and the function was therefore applied to the current datasets since the sectioning step size is different than the pixel size of the SEM images. For every voxel of the reconstructed volume, the 3-D EDT algorithm finds the largest possible spherical pore that holds that voxel. The number of voxels with the same diameter corresponds to a given pore size class. The table of pore volume versus pore size class for a reconstructed 3-D volume is thus obtained. The porosity of the sample is obtained by dividing the total 3-D pore volume by the total volume of the sample domain.

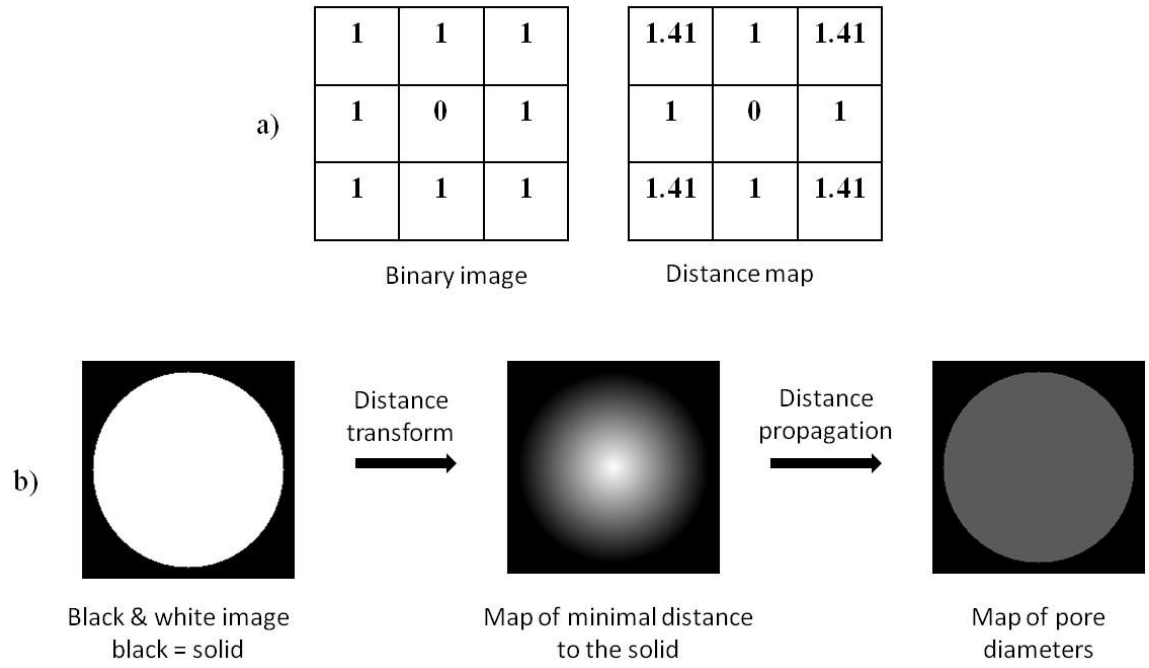

Figure 2.6. Example of a) Euclidean distance and b) Euclidean distance transform (EDT) algorithm applied to a 2-D circular pore.

The porosity of MPL is commonly estimated by comparing the changes of porosimetry data of the bare GDL upon the application of an MPL to its surface. These measurements assume a range (~50-100 μm) for MPL thickness, which leads to a range (~0.4-0.6) of porosity values that is too wide to assess the accuracy of segmentation protocols. Therefore, in the present study, mercury intrusion porosimetry (MIP) data were

obtained for the pure MPL sample coated on a polyimide film. The sample was inserted into the penetrometer of a Micromeritics AutoPoreIII porosimeter and the air was removed to ensure all the pores within the sample were completely evacuated. The mercury was then introduced into the capillary tube at 1.47 psia and subsequently the pressure was increased incrementally to 24000 psia to obtain 10 nm mean diameter pores. The penetrometer measures the incremental and cumulative pore volumes normalized by the sample weight. The correlation between the intrusion equilibrium pressure (p_{eq}) and mean pore diameter (d) is given by the equation:

$$p_{eq} = -\frac{4\psi \cos\phi}{d} \tag{2.3}$$

where ψ is the surface tension and ϕ is the contact angle. The porosity of the sample obtained by the MIP measurements needs to account for the non-porous polyimide film. The MIP measurement of the blank film was therefore performed to decouple its impact on sample porosity and pore size distribution. Despite the film being a non-porous material, the MIP measurement detected mercury intrusion in the film. The mercury intrusion volume in the film can be attributed to space between the layers and irregular edges as a result of sample cutting performed prior to placing the sample into the penetrometer ("the edge effect").

2.4. Calculation of effective transport properties

The internal morphology plays a significant role in the transport phenomena in porous media. In the case of MPL, only limited knowledge on morphology is available and transport properties are therefore difficult to predict. The present MPL characterization framework, however, provides useful insight into the MPL morphology and a suitable platform for relatively accurate calculations of the MPL specific transport properties. The current study focuses on effective diffusivity, tortuosity, and thermal conductivity.

2.4.1. Effective diffusivity

The effective diffusivity, γ, is a non-dimensional, normalized quantity defined as the ratio of the effective diffusion coefficient of a diffusive species in a porous media, D_i^{eff}, to the bulk diffusion coefficient, D_i^b:

$$D_i^{eff} = \gamma D_i^b \tag{2.4}$$

For macro and microporous media such as GDL substrates, the above formula is sufficient to calculate the effective diffusivity based on bulk diffusion. Bulk diffusion occurs when collision between gas molecules is more likely than with the pore wall. However, for nanoporous media such as the present MPL, Knudsen effects must also be considered. Hence, the local diffusion coefficient, D_i is expressed as a function of the bulk diffusion (particle/particle collisions) and Knudsen diffusion (particle/wall collisions) coefficients [71]:

$$D_i = \left(\frac{1}{D_i^b} + \frac{1}{D_i^K}\right)^{-1} \tag{2.5}$$

where $D_i^K$is the local Knudsen diffusion coefficient is expressed as a function of the pore diameter:

$$D_i^K = \frac{d}{3}\sqrt{\frac{8RT}{\pi M_i}} \tag{2.6}$$

where d, R, T, and M_i are the local pore diameter, universal gas constant, temperature, and molar mass of the diffusing species. It is noteworthy that in contrast to regular bulk diffusion, the Knudsen and mixed diffusion regimes depend on the properties of individual molecules as well as the local pore morphology. For the MPL, oxygen is the primary species of interest and therefore reported here, although the calculation method is valid for any other diffusing species (*e.g.,* H_2, H_2O). The local pore morphology is conveniently obtained from the reconstructed MPL model, using the EDT algorithm described in section 2.3, to compute the local pore diameter.

The diffusion model was implemented using the finite element method (FEM) based commercial software package COMSOL® Multiphysics. The model was implemented using LiveLink™ for MATLAB® package which connects COMSOL® to the MATLAB® scripting environment. The MATLAB® scripting reduced the total runtime by automating the simulation setup and analysis process. The segmented image by itself can act as a finite element mesh, but mesh is further refined using the “hauto” function [72]. The “hauto” function has 9 predefined options to select the degree of mesh resolution from extremely fine to extremely coarse. The details about predefined mesh settings and mesh

element size parameters can be found in the COMSOL Multiphysics Programming Reference Manual [73]. Further the “hauto” function could be used to automate the convergence and mesh independence study. The diffusion model calculates the effective diffusivity based on subscale computational domains extracted from the reconstructed MPL models. The fixed concentration drop, Δc, was specified through Dirichlet boundary conditions on the top and bottom surfaces of the domain in the principal direction of diffusion, while symmetric boundary conditions were applied on the sides to prevent any net flux in the in-plane direction. No-flux boundary conditions were applied at the internal interfaces between the solid and pore phases. The diffusion equation was solved to compute the concentration field in the domain:

$$\nabla \cdot \left(-D_{O_2} \nabla c_{O_2}\right) = 0 \tag{2.7}$$

The effective diffusivity of the structure was then obtained by expressing the net flux through the structure, $\dot{J}$, as a function of the overall concentration gradient using Fick’s law:

$$\dot{J} = \gamma D_{O_2} \frac{\Delta C_{O_2}}{l} \tag{2.8}$$

where l is the directional thickness of the domain.

2.4.2. Tortuosity

The estimation of tortuosity of a material is not trivial, which is why a wealth of tortuosity calculation methods have been developed across multiple fields of research [74]: electrochemistry, geology, medicine, heating, ventilation, and air conditioning (HVAC), acoustics, etc. In geometrical terms, tortuosity, τ is defined as ratio of shortest convoluted path length through the porous medium, ΔL_c to the Euclidean distance between the starting and end point of that path, ΔL (Figure 2.7). As such, tortuosity, τ has value equal to or greater than unity.

$$\tau = \frac{\Delta L_c}{\Delta L} \tag{2.9}$$

From the above geometric perspective, the effect of conduction, advection and diffusion processes in a porous medium are not considered. To describe the structure of the fuel

cell electrodes, the concept of tortuosity is applied in a broader way than a simple geometric measure; tortuosity is used to quantify and describe the resistance of the electrode to a flux.

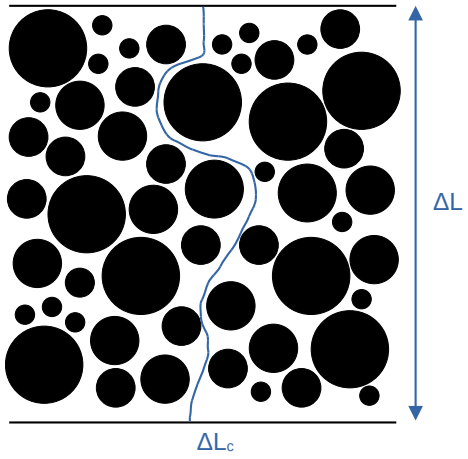

Figure 2.7. Illustration of a tortuous path through a porous structure.

Originally, Epstein differentiated between the 'geometric tortuosity' and 'tortuosity factor' using a capillary model [75]. Tortuosity factor accounts for additional path length and its effect on species diffusing through the porous media. To describe Knudsen transport in porous media, an effective diffusivity, D_i^{eff} is defined which relates the bulk diffusion coefficient (D_i^b), tortuosity (τ), and sample porosity (ε):

$$D_i^{eff} = \frac{\varepsilon}{\tau} \times D_i^b \qquad 2.10$$

The use of porosity-tortuosity relationship is one of the straightforward ways to deduce the tortuosity of the porous medium. The Bruggeman equation is the most widespread relation applied in the modeling of electrochemical devices [76]. The equation *2.11* presents the general form of the Bruggeman relationship, where α is the Bruggeman exponent, which in its standard form is equal to 1.5. The scaling factor, σ is the fitting parameter to fit the experimentally derived tortuosity data and is equal to 1 in the Bruggeman's original equation.

$$\tau_{Bruggeman} = \sigma \times \varepsilon^{(1-\alpha)} \qquad 2.11$$

The lack of detailed geometrical information related to the complex fuel cell electrode structure in 3-D had prevented the extraction of meaningful data on the tortuosity of the electrode materials. In absence of the 3-D structural information, tortuosity is experimentally derived by means of diffusion cell experiments and electrochemical measurements. The experimentally determined tortuosity values are valid only for a specific experiment at hand, as changes in operating conditions such as temperature, set-up and gas composition affect the results. Moreover, tortuosity is usually used as a fitting parameter in experimental data and hence depend on the chosen calculation method [77]. During the last decade relatively easy access to sophisticated tomography instruments has increased the availability of 3-D microstructural information and characterization techniques.

In image-based models the tortuosity is calculated by two main approaches: geometric-based and flux-based algorithms. The geometric based algorithm calculates the tortuosity of the porous material using equation *2.9*. The shortest pathway through the porous material is commonly determined by the pore centroid method [78] or the fast-marching method [79]. The flux-based method calculates tortuosity by considering flux-like behavior of transport phenomena through the porous material. Further, the flux-based algorithms are divided into voxel-based and mesh-based algorithms. In voxel-based approach the calculations are performed directly on the segmented voxel dataset of the reconstructed volume [80]. In mesh-based algorithm, a mesh is created for the segmented reconstructed volume before performing the tortuosity calculations. The mesh sensitivity analysis is carried out to decouple the influence of finite mesh on the tortuosity value. In this study, the finite element method was used to determine the flux in the reconstructed MPL samples as described in section 2.4.1. The tortuosity of the sample was calculated using equation *2.10*, which is equivalent to:

$$\tau = \left\{\frac{Volume\ averaged\ flux\ of\ homogeneous\ medium}{Volume\ averaged\ flux\ of\ heterogeneous\ model}\right\} \times (Volume\ fraction\ of\ the\ pore\ volume) \qquad 2.12$$

2.4.3. Effective thermal conductivity

The temperature distribution and heat transfer within the MPL depend upon its thermal conductivity. In the present study, the reconstructed MPL models were employed

together with a numerical algorithm to calculate the effective thermal conductivity of the solid phase of the structure. Provided that the carbon and PTFE components have different thermal conductivities and could not be distinguished by the images, an effective media approach was considered to estimate the feasible range of thermal conductivity. The upper bound (K_{max}) corresponds to a distribution of PTFE that provides the least possible thermal resistance, and vice versa for the lower bound (K_{min}):

$$K_{max} = \upsilon_{PTFE}\, K_{PTFE} + (1 - \upsilon_{PTFE})\, K_p \tag{2.13}$$

$$K_{min} = \left(\frac{\upsilon_{PTFE}}{K_{PTFE}} + \frac{1 - \upsilon_{PTFE}}{K_P}\right)^{-1} \tag{2.14}$$

where K_{PTFE} is the thermal conductivity of PTFE, K_P is the thermal conductivity of CB nanoparticle or CG/FG particle and υ_{PTFE} represent the volume fraction of PTFE. The steady state heat conduction equation was solved in COMSOL® Multiphysics for a predefined temperature drop, ΔT, applied to the domain boundaries in the heat transfer direction, like the procedure for diffusion calculation in section 2.4.1:

$$\nabla \cdot (-K\, \nabla T) = 0 \tag{2.15}$$

where K is the local thermal conductivity, in this case represented by either K_{max} or K_{min}. The corresponding heat flux $\dot{Q}$, quantified from the obtained temperature field was used to evaluate the effective thermal conductivity, K^{eff}, for both upper and lower bounds:

$$\dot{Q} = K^{eff}\left(\frac{\Delta T}{l}\right) \tag{2.16}$$

A summary of the methodology used to quantify the key structural parameters and effective transport properties of the MPL is provided in Figure 2.8.

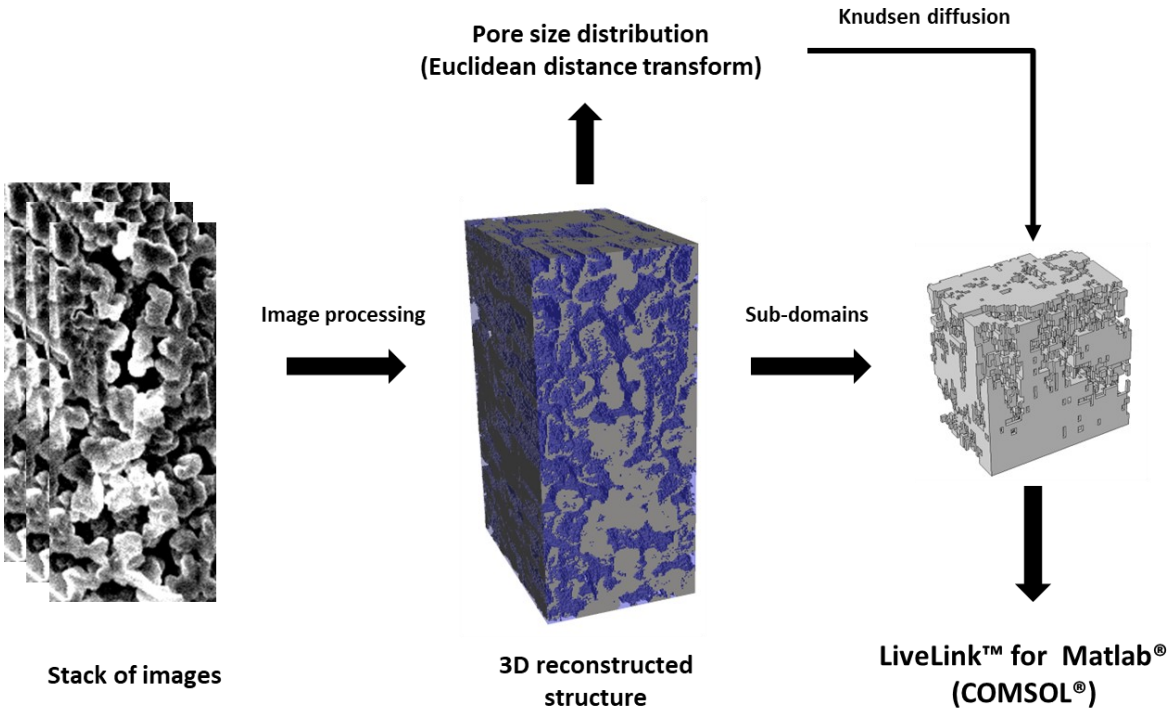

Figure 2.8. The framework used for quantification of structural parameters and effective transport properties.

Chapter 3.

Results and discussion

The 3-D reconstructed MPL models were obtained by the customized FIB-SEM based morphology characterization framework. Models were then used as the computational domain for the numerical algorithms to calculate the key structural parameters and effective transport properties of the MPL samples. The results obtained for pore size distribution, effective diffusivity, tortuosity, and effective thermal conductivity are summarized and discussed in the following sections.

Part of the material in this chapter is excerpted, changed, and reproduced with permission from the following paper that I co-authored:

"A Customized Framework for 3-D Morphological Characterization of Microporous Layers" Nanjundappa, A., et al., Electrochimica Acta 110 (2013), 349-357, 2013.

3.1. Porosity and pore size distribution

To calculate the porosity and PSD of the MPL, the proposed EDT algorithm was first analyzed. The algorithms for both 2-D and 3-D EDT implementation were considered; the 2-D approach was expected to be more economical and less time consuming, while the 3-D approach was expected to be more accurate considering the non-uniform structure of the MPL. The calculated PSD for CB MPL Domain 1 is shown in Figure 3.1 for 2-D and 3-D EDT. As can be seen, there are significant differences between the two EDT approaches. Although the curve shapes are similar, the 2-D EDT appears to consistently underestimate the pore size by 20–30 nm, on average. This difference is likely attributed to the high degree of pore connectivity in the MPL that is only captured by the 3-D approach, which is therefore advantageous for MPL studies despite being more computationally expensive. The 3-D reconstructed CB MPL domains have global porosity in the range of 62-65% in all three domains. In previous reports, the MPL porosity was estimated by comparing the changes of porosimetry data of a bare GDL substrate upon the application of an MPL to its surface [81]. These measurements assumed a range (~50–100 μm) for MPL thickness, which led to a range (~0.4–0.6) of porosity that is too wide to assess the accuracy of the segmentation protocols. Therefore, in the present

study, the MIP measurements for a pure MPL sample coated on a polyimide film resulted in a porosity of ~61%. The MIP porosity values obtained were adjusted to take into account the mercury intrusion in the polyimide film ("the edge effect"). The reconstructed 3-D structure obtained by the present FIB-SEM approach thereby appears to be a realistic representation of the expected solid and pore distribution of the physical MPL material.

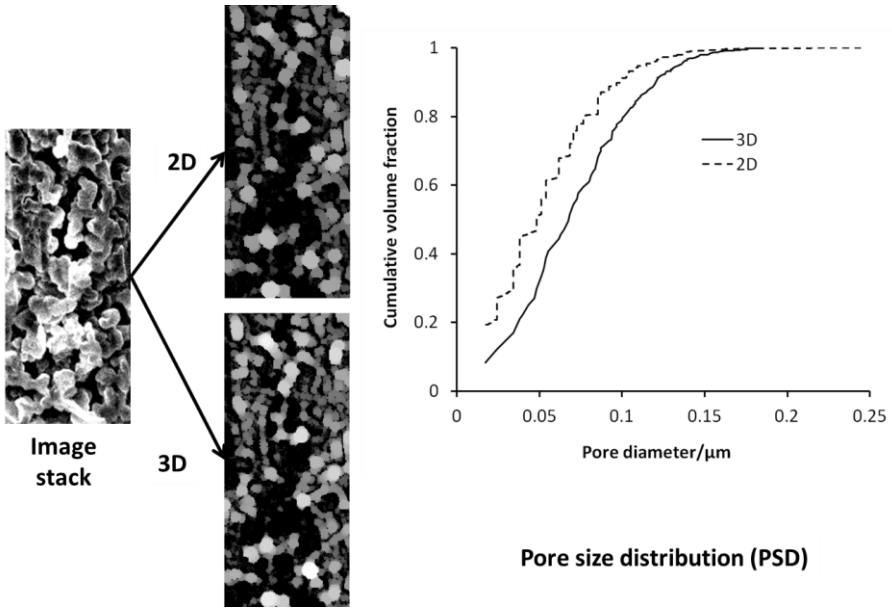

Figure 3.1. Difference between 2-D and 3-D Euclidean distance transform results for carbon black nanoparticle MPL Domain 1.

Figure 3.2 depicts the measured differential pore volume (DPV) and cumulative volume fraction (CVF) versus the pore diameter for CB MPL coated on polyimide film. The effective particle spacing for the CB nanoparticles results in two distinctive pore size regions. Figure 3.2 (a) shows the two regions, the first region with the distinctive peak (mode-1) around pore diameter of 100 nm and the second region with uncharacteristic peak around 1 µm (mode-2). The uncharacteristic peak around 1 µm is due to surface cracks and pores in the range of 1 to 60 µm (Figure 3.3). The surface cracks [28] and pores were formed during drying and sintering processes as a result of drastic changes in the volume of the MPL mixture. Further, the polyimide film's impact on PSD is observed for pore diameters above 10 µm. During the operation of the fuel cell it is likely that liquid water accumulates in these surface cracks and pores resulting in a decrease in fuel cell performance because of 'water flooding phenomena'. This can also contribute to membrane dehydration under low humidity operation [29]. Hence, having homogeneous

pore size distribution in the MPL structure may improve the performance and mechanical durability of the fuel cell [28]. Therefore, in the current study the RoI of the CB MPL sample was chosen to avoid the surface cracks and pores (Figure 3.3).

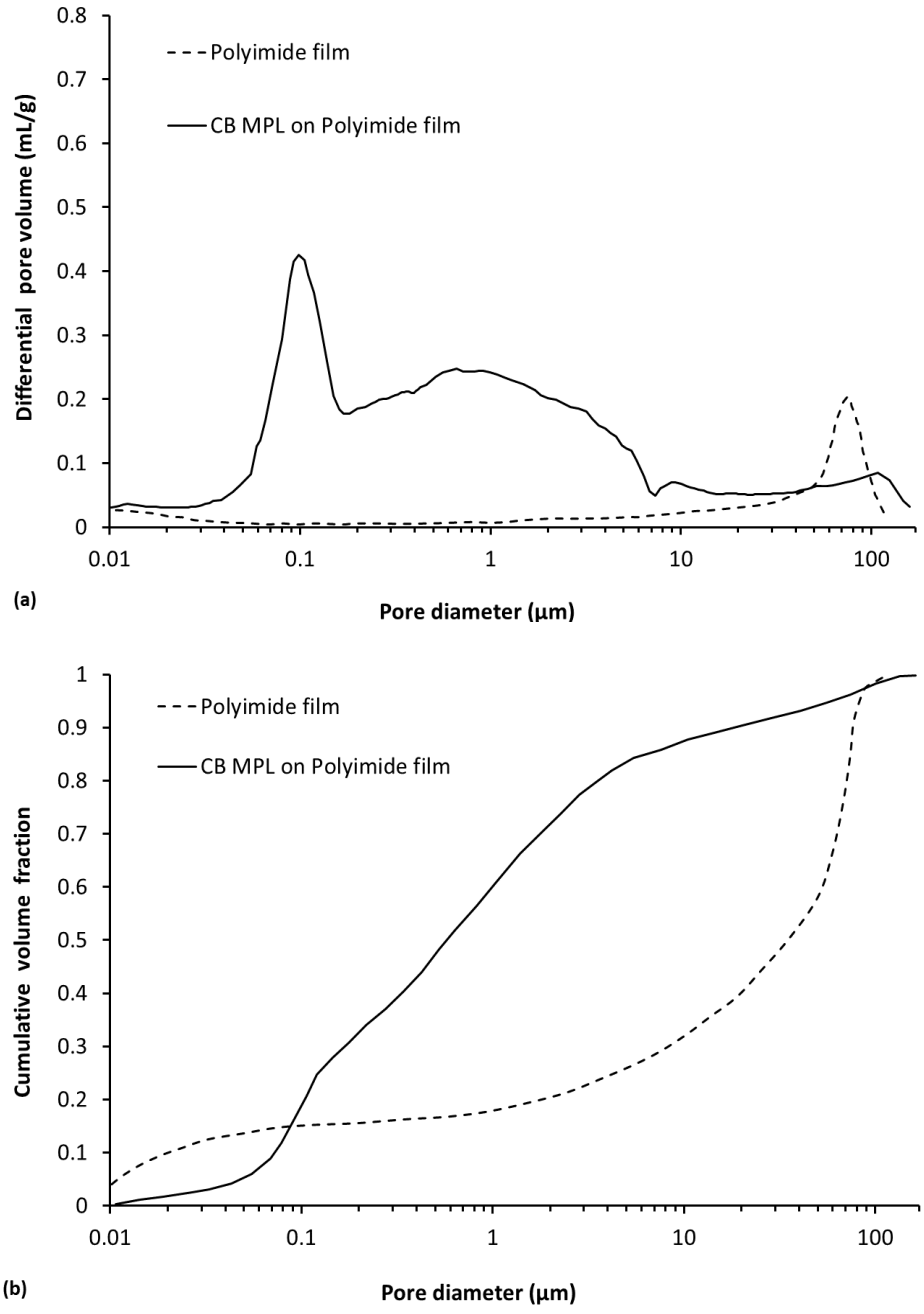

Figure 3.2. The measured a) differential pore volume and b) cumulative volume fraction as a function of pore diameter for CB MPL coated on polyimide film.

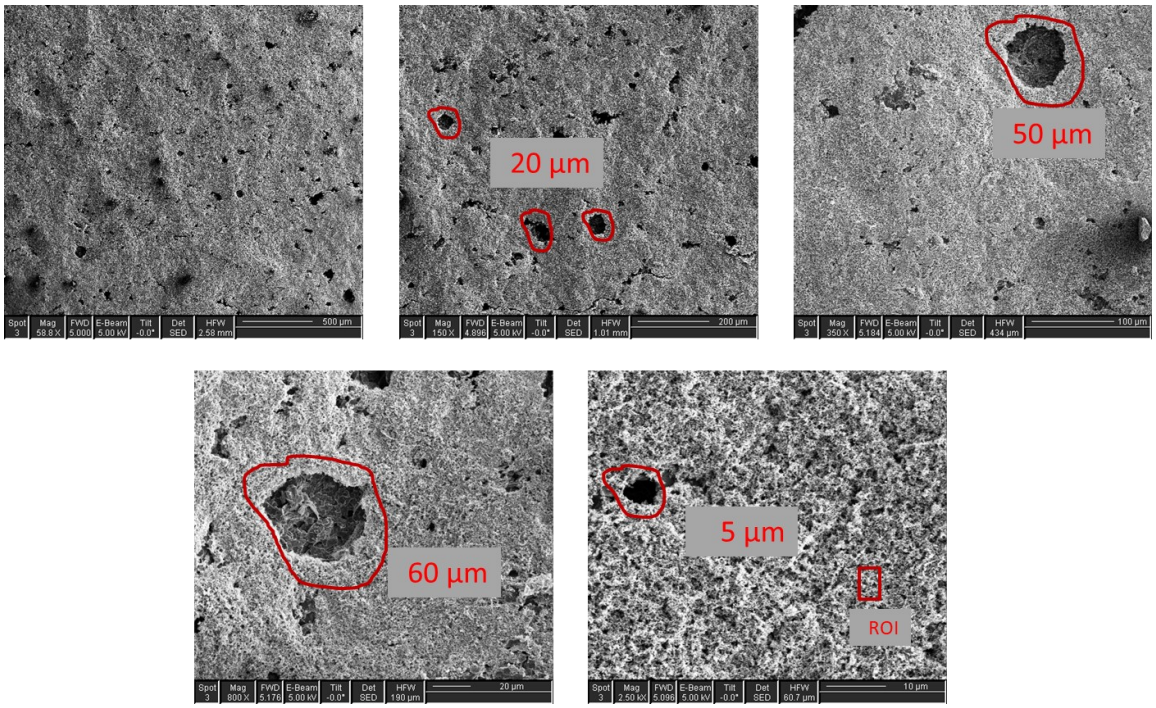

Figure 3.3. The surface cracks and pores on the CB MPL samples.

The PSD obtained for all three MPL domains using the 3-D EDT and the measured MIP data for a pure MPL sample coated on a blank polyimide film are provided in Figure 3.4. All three domains are shown to have similar PSD and the obtained curves agree reasonably well, on average, with the measured data across the entire range considered. The slight variations with the measured data can be attributed to the fact that PSD obtained by MIP assumes cylindrical pore shape with a circular opening; hence, MIP measurements tend to slightly overestimate the volume occupied by small pores in the case where larger pores are only accessible through smaller ones (throat effect [44]). Most MPL pores are found to be between 20 and 300 nm in diameter. Domain 3 had somewhat smaller typical pore size than the other two domains, although the small difference detected here is likely a result of the regular material variability expected to be present in the MPL. The Knudsen number defined as the mean free path of the diffusing species (*i.e.,* oxygen) divided by the characteristic length (*i.e.,* mean pore diameter) was found to be on the order of ~1, thus within the transition regime between continuum and molecular diffusion. Therefore, particle/wall collisions cannot be neglected, and Knudsen effects must be considered when estimating the transport properties of the MPL.

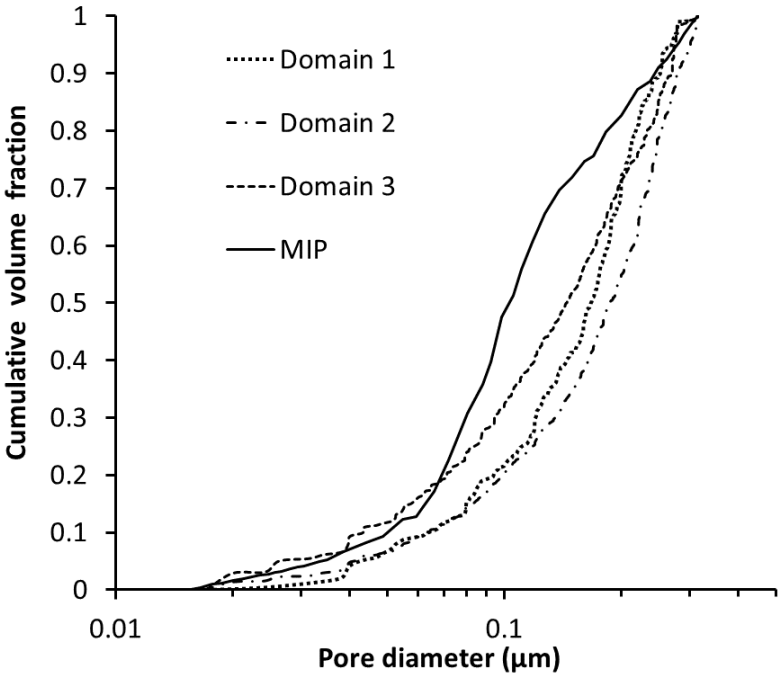

Figure 3.4. Pore size distribution obtained by the FIB-SEM based image reconstruction and Euclidean distance transform method compared to MIP data for a CB MPL coated on a blank substrate.

Figure 3.5 depicts the measured DPV and CVF versus the pore diameter for FG and CG MPLs coated on polyimide film. It is observed from the DPV measurements that the FG MPL sample follows unimodal distribution of pore diameter whereas the CG MPL sample follows bimodal distribution. Table 3.1 summarizes the characteristic pore diameters and the average particle size for the three MPL samples studied. It is observed that the average graphite particle size of 6 µm corresponds to CG MPL sample results in bimodal distribution (mode-1 and mode-2) of pore diameter. The bimodal distribution was also observed for graphite particles with sizes up to tens of micrometer (23 µm) [82]. The integrated pore volume under the mode-1 peak is almost equal for the FG and CG MPL samples, which is likely due to solvent evaporation during the drying and sintering processes. Whereas the mode-2 for CG MPL sample is due to the effective particle spacing of the microstructure, it is noteworthy that the FG MPL sample did not exhibit a mode-2 peak, which is likely due to its relatively small graphite particle size. Table 3.2 compares the global porosity value for the three samples studied using 3-D FIB-SEM reconstructed model and MIP measurements. The porosity values obtained from the 3-D FIB-SEM reconstructed model were 4-5% lower than the MIP measured data for the FG

and CG MPL samples, which is an acceptable difference considering the much smaller domain size of the model, which does not capture large pores. In addition to the smaller domain size, the underestimation of porosity value for the FG and CG MPL may be due to an increase in the amount of re-deposited material under higher ion-beam currents. As noted earlier (section 2.1) the beam current of 50 pA for FG MPL sample and 100 pA CG MPL sample were used to reduce the time and cost of image acquisition. Also, for the CG MPL sample the small domain size directly resulted in not resolving the mode-2 (Figure 3.6). Overall, the PSD of the model is in good agreement with the MIP data for the characteristic mode-1 pores for both FG and CG MPL samples. These pores are expected to dominate the pore phase transport properties of these materials.

Table 3.1. The characteristic pore diameters and average particle size for the three MPL samples.

Sample	Mode-1 (μm)	Mode-2 (μm)	Average particle size (μm)
CB	0.1	1	0.04
FG	0.27	Not applicable	2
CG	0.65	3.8	6

Table 3.2. The sample porosity value for the three MPL samples obtained using 3-D FIB-SEM reconstructed model and MIP measurements.

Samples	MIP	FIB-SEM
CB	61%	63%
FG	53%	49%
CG	53%	48%

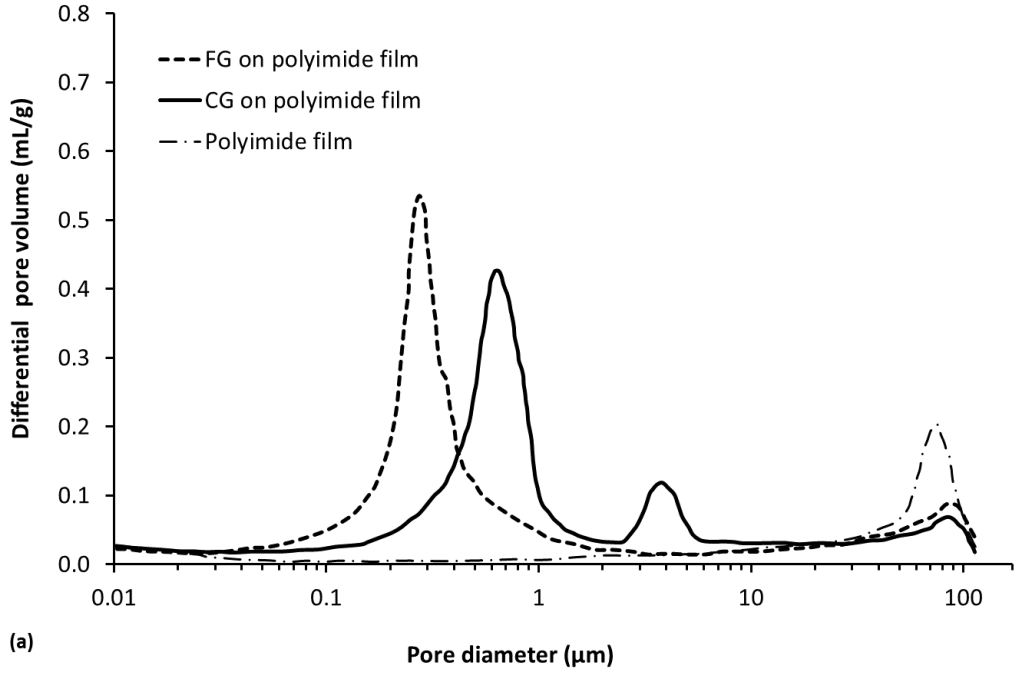

(a)

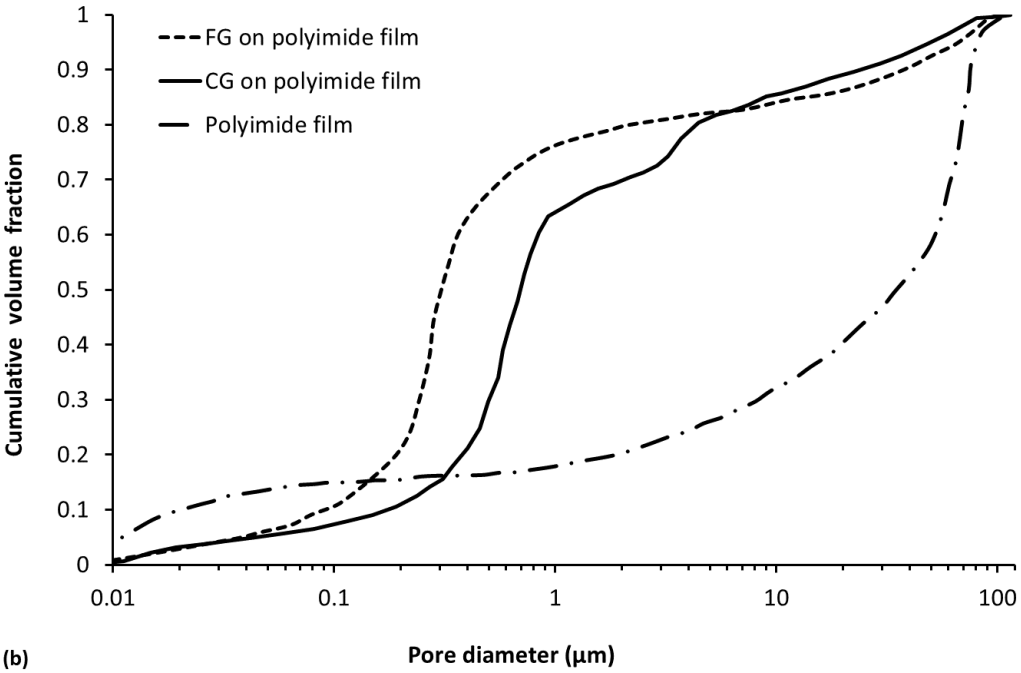

(b)

Figure 3.5 **The measured a) differential pore volume and b) cumulative volume fraction as a function of pore diameter for FG and CG MPLs coated on polyimide film.**

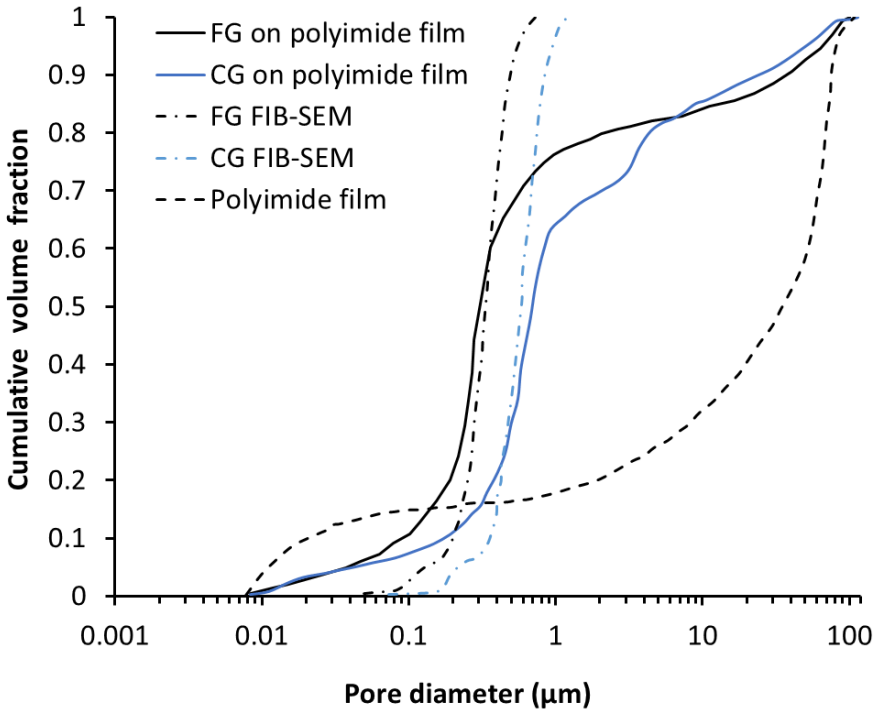

Figure 3.6. Pore size distribution obtained by the 3-D FIB-SEM reconstructed model and MIP data for the FG and CG MPL samples.

3.2. Effective transport properties

The calculated effective diffusivity of oxygen in air for the three domains of the CB MPL sample is depicted in Figure 3.7a. The effective diffusivity is presented in the three principal directions, namely the through-plane (TP), in-plane (IP), and sectioning directions (SD). The average effective diffusivity is found to be between 0.15 and 0.22 for the global porosity of 62–65% in all three domains. Although the average values vary among the three principal directions, the difference is within the variability of each dataset. Hence, the diffusion characteristics of the MPL are determined to be isotropic, with an average effective diffusivity of 0.18. The choice of sectioning direction, which is mutually perpendicular for Domains 2 and 3, also has no statistical influence on the results. The multi-domain strategy was also carried out to negate any effect of the ion beam milling and sectioning step size on the obtained structural parameters. The tuned MPL characterization framework thus appears to provide reliable results for diffusion.

In a previous FIB-SEM based study [59], the effective diffusivity of the reconstructed MPL structure with 40% porosity was estimated to ~0.18 based on the Tomadakis and Sotirchos method [83]. In another study, the model based on finite volume approximation to solve Fickian diffusion in a 3-D FIB-SEM generated structure with 42% porosity reported effective diffusivity values from 0.12 to 0.35 within the structure. Although the literature data for effective diffusivity are comparable to the present results, the previously reported values were likely overestimated due to the use of empirical correlations with limited applicability [59] and neglecting Knudsen diffusion [60] but augmented because of the low porosities. As mentioned in the introduction, MPL is not a standalone layer and measurements are normally carried out using a GDL/MPL assembly. Chan *et al.* [42] reported the measured diffusivity coefficient of oxygen–nitrogen mixture as 0.073 for an MPL coated on SolviCore carbon paper. A series network resistance was used for the estimation, although the precise thickness and penetration depth of the MPL were not taken into account.

The calculated tortuosity values for the CB MPL sample domains are given in Figure 3.7b and the average tortuosity is about 3.6. The overall trends are consistent with those found for diffusivity. PEM fuel cell models often use empirical models to determine the effective diffusivity as a function of bulk material properties such as porosity and tortuosity; the most common one being the Bruggeman relation (Equation *2.11*). The Bruggeman approximation of effective diffusivity and tortuosity for CB MPL material resulted in values of 0.48 and 1.27, respectively. These estimates are in considerable disagreement with those of the reconstructed FIB-SEM 3-D models, questioning the validity of the Bruggeman approximation in describing transport phenomena in the MPL structure.

The effective thermal conductivity obtained for the three CB MPL domains is displayed in Figure 3.8. Figure 3.8a represents the upper bound with an average of ~0.29 W m^{-1} K^{-1} and Figure 3.8b indicates the lower bound with ~0.13 W m^{-1} K^{-1} on average. The exact effective thermal conductivity of the material is somewhere within these bounds, depending on the PTFE distribution; however, the obtained range of 0.1–0.3 W m^{-1} K^{-1} is expected to be realistic and useful. One other study has reported thermal conductivity of 0.6 W m^{-1} K^{-1} for a bare MPL with lower porosity of 50% and lower PTFE content of 22% [55]. As mentioned earlier, there is significant variation within the reported experimental values of the MPL thermal conductivity, ranging from 0.04 – 4 W m^{-1} K^{-1}, due to the

complexity of the measurements, the presence of thermal contact resistance, and the uncertainty associated with the influence of (and coupling with) the GDL substrate.

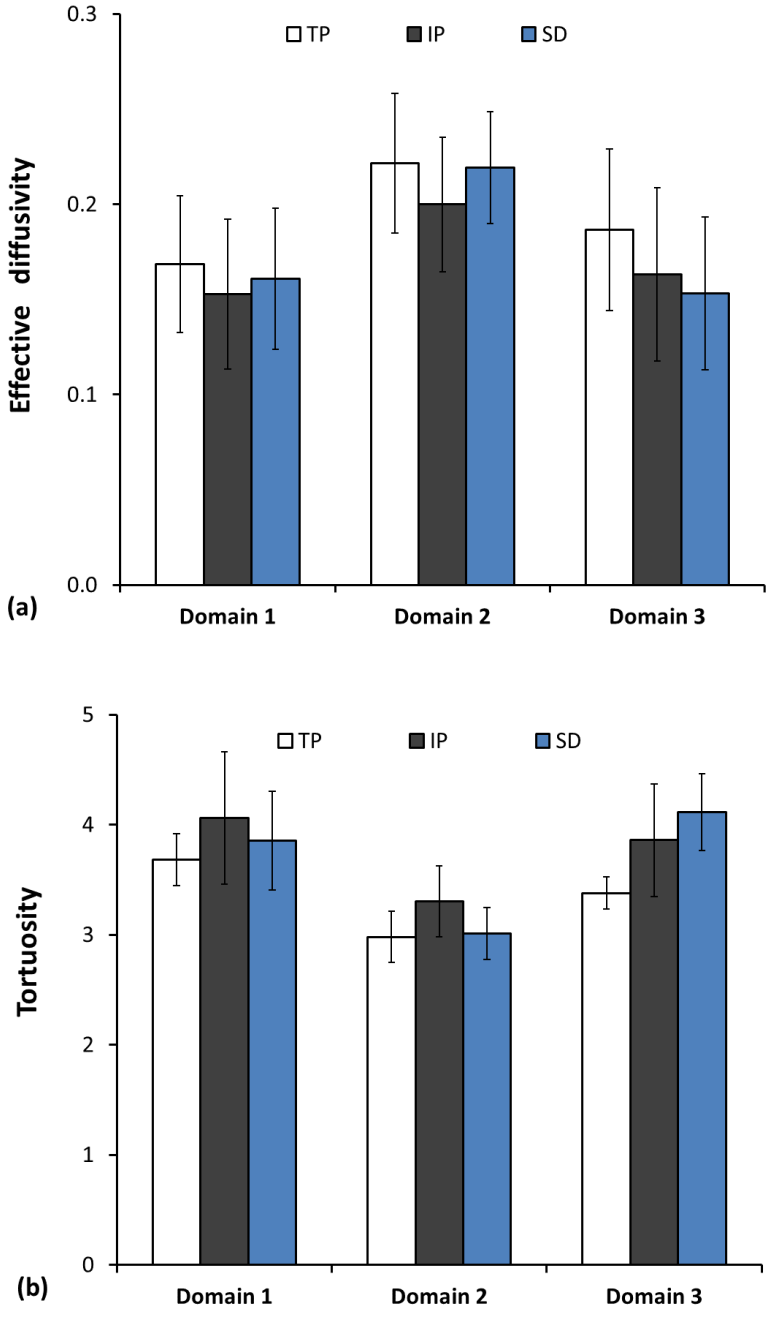

Figure 3.7. **(a) Effective diffusivity and (b) tortuosity obtained for the three reconstructed domains for the CB MPL sample in the through-plane (TP), in-plane (IP), and sectioning directions (SD).**

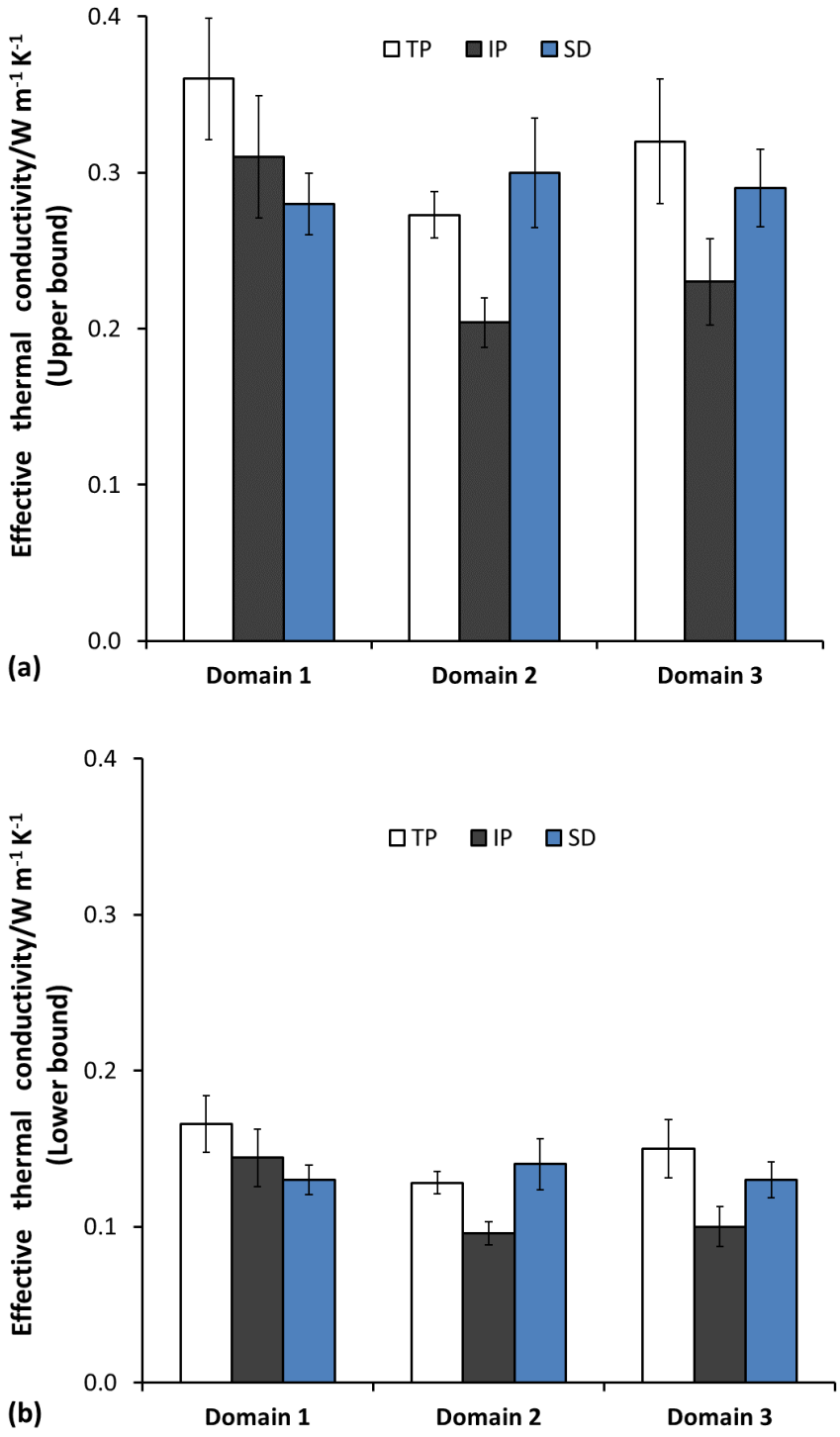

Figure 3.8. Effective thermal conductivity obtained for the three CB MPL domains in the through-plane (TP), in-plane (IP), and sectioning directions (SD), indicating (a) upper bound and (b) lower bound.

Figure 3.9a compares the calculated effective diffusivity of the CB MPL sample with that of the FG and CG MPL samples. The graphite particles in both FG and CG samples have uniform distribution across the surface with no visible surface cracks or pores (Figure 2.1). The thin platelet shaped graphite particles tend to stack with preferential orientation horizontally along the two mutually perpendicular in-plane directions. Furthermore, the layered stacking of graphite particles in the through-plane direction leads to an interconnected pore network throughout the microstructure. Within the variability of the dataset, the effectivity diffusivity value for the FG MPL sample in the in-plane directions (~0.135) is about twice that of the through-plane direction (~0.06). Hence, the diffusion characteristics of the FG MPL are determined to be transversely isotropic. However, the effective diffusivity values for CG MPL sample showed less distinct difference between the IP and TP directions (Figure 3.9a). The calculated tortuosity values for the FG and CG samples follow a similar trend as that of diffusivity (Figure 3.9b). The tortuosity value for the FG MPL sample (Figure 3.9b) in the in-plane directions (~8.0) is twice that of the through-plane direction (~3.7). The tortuosity values for the CG MPL sample in the three mutually perpendicular directions are 6 (TP), 3 (IP) and 5 (SD). The anisotropy exhibited by the CG MPL sample may be due to the larger particle size when compared to the FG sample. The anisotropy of the CG sample can also be attributed to the heterogeneous nature of the microstructure as observed in the PSD (Figure 3.5). Hence, the diffusion and tortuosity characteristics of the CG MPL are determined to be anisotropic.

The effective thermal conductivity obtained for the three MPL samples namely CB, FG, and CG are displayed in Figure 3.10. The intrinsic thermal conductivity of graphite particles is about two orders of magnitude higher than that of CB nanoparticles. Therefore, the gap in effective thermal conductivity between the CB MPL sample and the FG and CG MPL samples is more pronounced in the upper bound values (Figure 3.10a) when compared to the lower bound values (Figure 3.10b). The exact effective thermal conductivity of the FG and CG MPL samples is somewhere within the upper and lower bounds, depending on the PTFE distribution. The true values are likely to be closer to the upper bound values due to the planar stacking of graphite particles and relatively low PTFE content. The upper bound effectivity thermal conductivity value for the FG MPL sample in the in-plane directions (50 W m^{-1} K^{-1}) is about 40% higher that of the through-plane direction (35 W m^{-1} K^{-1}). The effective thermal conductivity values for the FG MPL

sample show similar trends as seen in the effective diffusivity and tortuosity values. The upper bound effectivity thermal conductivity value for the CG MPL sample in the three mutually perpendicular directions are 42 W m^{-1} K^{-1} (TP), 57 W m^{-1} K^{-1} (IP) and 41 W m^{-1} K^{-1} (SD). The effective thermal conductivity value for the CG MPL sample show slightly less anisotropy when compared to the effective diffusivity and tortuosity values. To the best of the author's knowledge, no similar imaging based studies have been previously reported for a graphite particle based MPL, and detailed validation of the results is difficult. The graphite particle MPLs effective thermal conductivity is about 150 times higher than that of the CB MPL sample. The higher thermal conductivity MPLs aids in removal of water under high current density operation leading to improved fuel cell performance (inhibiting "water flooding" phenomena). In sum, the range of effective transport properties found by the present approach is likely realistic for the MPL structure based on CB nanoparticle as well as graphite particles under 4 μm size and the findings may be useful as a benchmark for future research in this field.

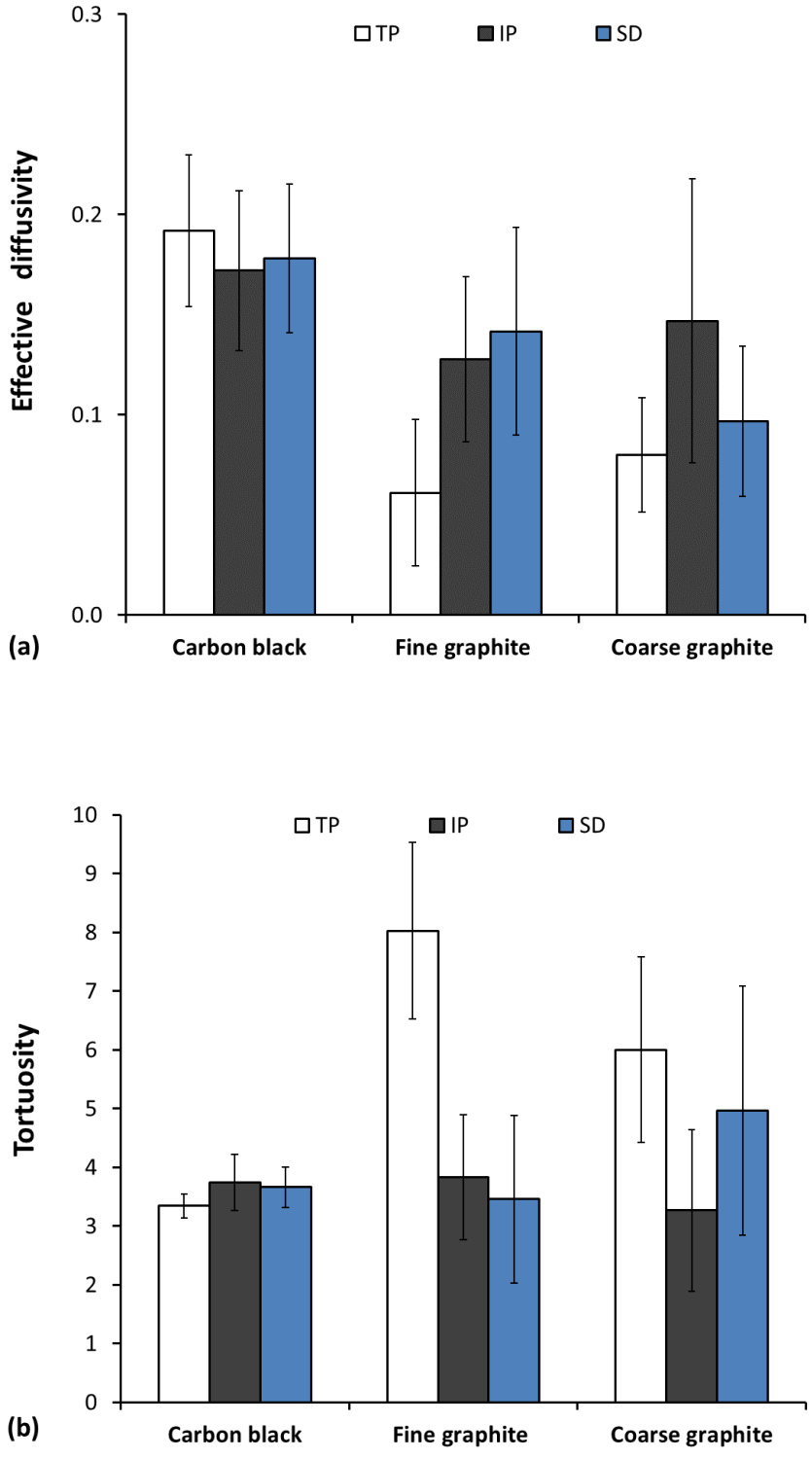

Figure 3.9. **(a) Effective diffusivity and (b) tortuosity obtained for the CB, FG, and CG MPL samples in the through-plane (TP), in-plane (IP), and sectioning directions (SD).**

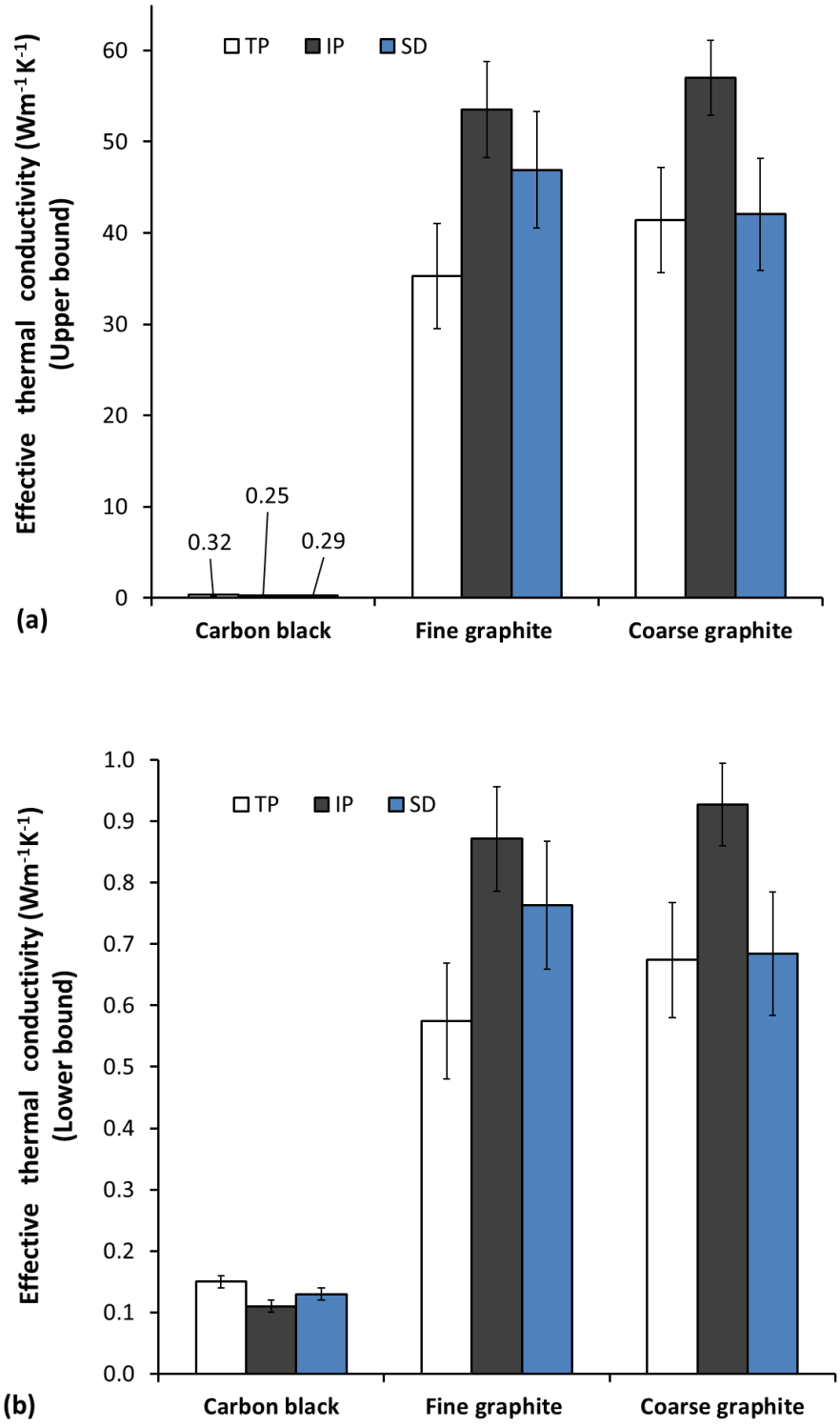

Figure 3.10. Effective thermal conductivity obtained for the CB, FG, and CG MPL samples in the through-plane (TP), in-plane (IP), and sectioning directions (SD), indicating (a) upper bound and (b) lower bound.

Chapter 4.

Conclusions and future work

The overall aim of this thesis was to evaluate the microstructure and related transport characteristics for two types of MPL materials based on spherical CB nanoparticles and disc-like graphite particles. To carry out this goal, a complete, customized framework for morphological characterization of MPLs was developed and presented. For this purpose, the real 3-D reconstructed structure of the MPL was obtained by capturing high-resolution images using a tuned FIB-SEM tomography method developed specifically for analysis of bare MPL samples with minimal sample preparation and other interferences. A suitable segmentation protocol for obtaining 3-D reconstructed structures was established. The porosity and pore size distribution calculated using a novel algorithm based on Euclidian distance transform, were found to be in good agreement with measured data for the MPLs coated on a blank substrate.

The key material properties of the MPL considered in this study, namely effective diffusivity, tortuosity, and effective thermal conductivity, were obtained from reconstructed MPL models representing three different domains of the CB MPL sample to analyze the impact of ion beam sectioning step size and direction. With the customized characterization approach, the milling parameters were found to have no significant bias on the results. Moreover, the obtained data for the CB MPL sample showed the microstructure as isotropic with respect to all structural parameters considered. The obtained CB MPL structure's effective diffusivity of ~0.18 and tortuosity of ~3.6 are believed to be much more realistic than estimations based on the Bruggeman approximation and other empirical correlations, due to their limited applicability for MPLs. The obtained data for the FG MPL sample shows the microstructure as transversely isotropic with respect to all structural parameters considered. The deduced structural parameters for the CG MPL sample shows the microstructure as anisotropic. The anisotropy can be attributed to larger particle size compared to the FG MPL sample and the heterogeneous microstructure seen in the PSD.

Also, for the first time, the effective thermal conductivity of a graphite particle based MPL was reported using the present characterization framework. The true values of

effective thermal conductivity of graphite particle MPLs are likely to be closer to the upper bound values because of TP stacking of graphite particles and low PTFE content of 18%. The upper bound effectivity thermal conductivity value for the FG MPL sample in the in-plane directions (50 W m^{-1} K^{-1}) is about 40% higher that of the through-plane direction (35 W m^{-1} K^{-1}). Whereas the effective thermal conductivity of the CB MPL sample is found to be within the range of 0.1–0.3 W m^{-1} K^{-1}. The FG and CG MPLs effective thermal conductivity is about 150 times higher than that of the CB MPL sample. The current study elucidates the importance of rigorous estimation of the key structural parameters, and it is expected that the customized characterization framework as well as the obtained material properties that are otherwise difficult to measure will find widespread application in the fuel cell research community in the areas of modeling, material development, and MEA design.

The use of water-soluble binder in the MPL mixture could prevent the formation of surface cracks and pores on the surface of the CB MPL sample. Further can address the impact of surface cracks and pores on the performance and mechanical durability of the fuel cell.

The use of low energy nano-XCT could resolve the mode-2 of PSD for CG MPL sample and could also potentially differentiate between graphite particle and PTFE phases, subject to resolution limitations. The use of a low energy laser cutter for preparing the sample needed for nano-XCT analysis would reduce the sample preparation time when compared to the Ga ion FIB lift-out technique.

The xenon (Xe) ion plasma FIBs higher current and higher sputtering rate could resolve the mode-2 of PSD for CG MPL sample. Xe ion plasma FIB could also reduce the sample preparation time for nano-XCT analysis when compared to the Ga ion FIB lift-out technique [84]. Further investigation is necessary to quantify the Xe ion plasma FIB induced artifacts on MPL and compare it to Ga ion FIB.

The obtained 3-D FIB-SEM reconstructed dataset may also serve as a training dataset for convolutional neural network (CNN) models. The CNN would reduce the dependency on the highly time consuming manual segmentation approach and could handle larger datasets. A well trained CNN model could reduce the image processing time by automating the image classification and image segmentation steps [85].

References

[1] Z. Qi, A. Kaufman, Improvement of water management by a microporous sublayer for PEM fuel cells, Journal of Power Sources. 109 (2002) 38–46. https://doi.org/10.1016/S0378-7753(02)00058-7.

[2] M.M. Mench, Thermodynamics of Fuel Cell Systems, in: Fuel Cell Engines, John Wiley & Sons, Ltd, 2008: pp. 62–120. https://doi.org/10.1002/9780470209769.ch3.

[3] T.E. Springer, T.A. Zawodzinski, S. Gottesfeld, Polymer Electrolyte Fuel Cell Model, Journal of The Electrochemical Society. 138 (1991) 2334–2342. https://doi.org/10.1149/1.2085971.

[4] Y. Liu, M. Murphy, D. Baker, W. Gu, C. Ji, J. Jorne, H.A. Gasteiger, Determination of Electrode Sheet Resistance in Cathode Catalyst Layer by AC Impedance, ECS Transactions. 11 (2007) 473–484. https://doi.org/10.1149/1.2780961.

[5] N. Zamel, X. Li, Effective transport properties for polymer electrolyte membrane fuel cells - with a focus on the gas diffusion layer, Progress in Energy and Combustion Science. 39 (2013) 111–146.

[6] A.Z. Weber, J. Newman, Modeling transport in polymer-electrolyte fuel cells, Chemical Reviews. 104 (2012) 4679–4726. https://doi.org/10.1021/cr020729l.

[7] Z. Zhan, J. Xiao, Y. Zhang, M. Pan, R. Yuan, Gas diffusion through differently structured gas diffusion layers of PEM fuel cells, International Journal of Hydrogen Energy. 32 (2007) 4443–4451.

[8] C.-Y. Wang, Fundamental models for fuel cell engineering, Chemical Reviews. 104 (2012) 4727–4766. https://doi.org/10.1021/cr020718s.

[9] Mathias M, Roth J, Fleming J, Lehnert W, Diffusion media materials and characterization, handbook of fuel cells-fundamentals, technology and applications, John Wiley and Sons, 2003.

[10] K. Jiao, J. Xuan, Q. Du, Z. Bao, B. Xie, B. Wang, Y. Zhao, L. Fan, H. Wang, Z. Hou, S. Huo, N.P. Brandon, Y. Yin, M.D. Guiver, Designing the next generation of proton-exchange membrane fuel cells, Nature (London). 595 (2021) 361–369.

[11] A. Ozden, S. Shahgaldi, X. Li, F. Hamdullahpur, A review of gas diffusion layers for proton exchange membrane fuel cells—With a focus on characteristics, characterization techniques, materials and designs, Progress in Energy and Combustion Science. 74 (2019) 50–102. https://doi.org/10.1016/j.pecs.2019.05.002.

[12] T.E. Springer, T.A. Zawodzinski, M.S. Wilson, S. Gottesfeld, Characterization of polymer electrolyte fuel cells using AC impedance spectroscopy, Journal of The Electrochemical Society. 143 (1996) 587–599. https://doi.org/10.1149/1.1836485.

[13] D.R. Baker, C. Wieser, K.C. Neyerlin, M.W. Murphy, The use of limiting current to determine transport resistance in PEM fuel cells, ECS Transactions. 3 (2006) 989–999. https://doi.org/10.1149/1.2356218.

[14] D. Kramer, S.A. Freunberger, R. Flükiger, I.A. Schneider, A. Wokaun, F.N. Büchi, G.G. Scherer, Electrochemical diffusimetry of fuel cell gas diffusion layers, Journal of Electroanalytical Chemistry. 612 (2008) 63–77.

[15] R. Flückiger, S.A. Freunberger, D. Kramer, A. Wokaun, G.G. Scherer, F.N. Büchi, Anisotropic, effective diffusivity of porous gas diffusion layer materials for PEFC, Electrochimica Acta. 54 (2008) 551–559.

[16] C. Quick, D. Ritzinger, W. Lehnert, C. Hartnig, Characterization of water transport in gas diffusion media, Journal of Power Sources. 190 (2009) 110–120.

[17] A. Casalegno, L. Colombo, S. Galbiati, R. Marchesi, Quantitative characterization of water transport and flooding in the diffusion layers of polymer electrolyte fuel cells, Journal of Power Sources. 195 (2010) 4143–4148.

[18] N. Zamel, N.G.C. Astrath, X. Li, J. Shen, J. Zhou, F.B.G. Astrath, H. Wang, Z.-S. Liu, Experimental measurements of effective diffusion coefficient of oxygen nitrogen mixture in PEM fuel cell diffusion media, Chemical Engineering Science. 65 (2010) 931–937.

[19] J.M. LaManna, S.G. Kandlikar, Determination of effective water vapor diffusion coefficient in pemfc gas diffusion layers, International Journal of Hydrogen Energy. 36 (2011) 5021–5029.

[20] K. Schladitz, S. Peters, D. Reinel-Bitzer, A. Wiegmann, J. Ohser, Design of acoustic trim based on geometric modeling and flow simulation for non-woven, Computational Materials Science. 38 (2006) 56–66.

[21] C. Redenbach, K. Schladitz, I. Vecchio, O. Wirjadi, Image analysis for microstructures based on stochastic models, GAMM-Mitteilungen. 37 (2014) 281–305. https://doi.org/10.1002/gamm.201410013.

[22] M. Godehardt, A. Moghiseh, C. Oetjen, J. Ohser, K. Schladitz, An unambiguous cloudiness index for nonwovens, Journal of Mathematics in Industry. 12 (2022) 9. https://doi.org/10.1186/s13362-022-00124-z.

[23] V.P. Schulz, J. Becker, A. Wiegmann, P.P. Mukherjee, C.-Y. Wang, Modeling of two-phase behavior in the gas diffusion medium of PEFCs via full morphology approach, Journal of The Electrochemical Society. 154 (2007) B419–B426. https://doi.org/10.1149/1.2472547.

[24] P.K. Sinha, P.P. Mukherjee, C.-Y. Wang, Impact of GDL structure and wettability on water management in polymer electrolyte fuel cells, Journal of Materials Chemistry. 17 (2007) 3089–3103.

[25] Z. Tayarani-Yoosefabadi, D. Harvey, J. Bellerive, E. Kjeang, Stochastic microstructural modeling of fuel cell gas diffusion layers and numerical

determination of transport properties in different liquid water saturation levels, Journal of Power Sources. 303 (2016) 208–221. https://doi.org/10.1016/j.jpowsour.2015.11.005.

[26] M.E. Hannach, E. Kjeang, Stochastic Microstructural Modeling of PEFC Gas Diffusion Media, Journal of The Electrochemical Society. 161 (2014) F951–F960. https://doi.org/10.1149/2.1141409jes.

[27] P.P. Mukherjee, C.-Y. Wang, X. Li, Polymer electrolyte fuel cell modeling – a pore-scale perspective green energy, in: Springer London, 2011: pp. 181–221.

[28] J.H. Chun, D.H. Jo, S.G. Kim, S.H. Park, C.H. Lee, S.H. Kim, Improvement of the mechanical durability of micro porous layer in a proton exchange membrane fuel cell by elimination of surface cracks, Renewable Energy. 48 (2012) 35–41. https://doi.org/10.1016/j.renene.2012.04.011.

[29] A. Ozden, S. Shahgaldi, X. Li, F. Hamdullahpur, A graphene-based microporous layer for proton exchange membrane fuel cells: Characterization and performance comparison, Renewable Energy. 126 (2018) 485–494. https://doi.org/10.1016/j.renene.2018.03.065.

[30] A.Z. Weber, J. Newman, Effects of microporous layers in polymer electrolyte fuel cells, Journal of The Electrochemical Society. 152 (2005) A677–A688. https://doi.org/10.1149/1.1861194.

[31] H.K. Atiyeh, K. Karan, B. Peppley, A. Phoenix, E. Halliop, J. Pharoah, Experimental investigation of the role of a microporous layer on the water transport and performance of a PEM fuel cell, Journal of Power Sources. 170 (2007) 111–121.

[32] J.T. Gostick, M.A. Ioannidis, M.W. Fowler, M.D. Pritzker, On the role of the microporous layer in PEMFC operation, Electrochemistry Communications. 11 (2009) 576–579.

[33] J. Becker, C. Wieser, S. Fell, K. Steiner, A multi-scale approach to material modeling of fuel cell diffusion media, International Journal of Heat and Mass Transfer. 54 (2011) 1360–1368.

[34] M.E. Hannach, R. Singh, N. Djilali, E. Kjeang, Micro-porous layer stochastic reconstruction and transport parameter determination, Journal of Power Sources. 282 (2015) 58–64. https://doi.org/10.1016/j.jpowsour.2015.02.034.

[35] S.F. Burlatsky, V.V. Atrazhev, M. Gummalla, D.A. Condit, F. Liu, The impact of thermal conductivity and diffusion rates on water vapor transport through gas diffusion layers, Journal of Power Sources. 190 (2009) 485–492.

[36] G. Karimi, X. Li, P. Teertstra, Measurement of through-plane effective thermal conductivity and contact resistance in PEM fuel cell diffusion media, Electrochimica Acta. 55 (2010) 1619–1625.

[37] P. Teertstra, G. Karimi, X. Li, Measurement of in-plane effective thermal conductivity in PEM fuel cell diffusion media, Electrochimica Acta. 56 (2011) 1670–1675.

[38] G. Unsworth, N. Zamel, X. Li, Through-plane thermal conductivity of the microporous layer in a polymer electrolyte membrane fuel cell, International Journal of Hydrogen Energy. 37 (2012) 5161–5169.

[39] O.S. Burheim, H. Su, S. Pasupathi, J.G. Pharoah, B.G. Pollet, Thermal conductivity and temperature profiles of the micro porous layers used for the polymer electrolyte membrane fuel cell, International Journal of Hydrogen Energy. 38 (2013) 8437–8447. https://doi.org/10.1016/j.ijhydene.2013.04.140.

[40] A. Thomas, G. Maranzana, S. Didierjean, J. Dillet, O. Lottin, Thermal and water transfer in PEMFCs: Investigating the role of the microporous layer, International Journal of Hydrogen Energy. 39 (2014) 2649–2658. https://doi.org/10.1016/j.ijhydene.2013.11.105.

[41] O.S. Burheim, G.A. Crymble, R. Bock, N. Hussain, S. Pasupathi, A. du Plessis, S. le Roux, F. Seland, H. Su, B.G. Pollet, Thermal conductivity in the three layered regions of micro porous layer coated porous transport layers for the PEM fuel cell, International Journal of Hydrogen Energy. 40 (2015) 16775–16785. https://doi.org/10.1016/j.ijhydene.2015.07.169.

[42] C. Chan, N. Zamel, X. Li, J. Shen, Experimental measurement of effective diffusion coefficient of gas diffusion layer/microporous layer in PEM fuel cells, Electrochimica Acta. 65 (2012) 13–21.

[43] J.T. Gostick, M.W. Fowler, M.A. Ioannidis, M.D. Pritzker, Y.M. Volfkovich, A. Sakars, Capillary pressure and hydrophilic porosity in gas diffusion layers for polymer electrolyte fuel cells, Journal of Power Sources. 156 (2006) 375–387.

[44] P.Z. Wong, Experimental methods in the physical sciences: methods of the physics of porous media, Acad. Press, 1999.

[45] T. Soboleva, X. Zhao, K. Malek, Z. Xie, T. Navessin, S. Holdcroft, On the micro-, meso-, and macroporous structures of polymer electrolyte membrane fuel cell catalyst layers, ACS Applied Materials & Interfaces. 2 (2012) 375–384. https://doi.org/10.1021/am900600y.

[46] P.A. Webb, An Introduction to the Physical Characterization of Materials by Mercury Intrusion Porosimetry with Emphasis on Reduction and Presentation of Experimental Data, (2001). https://www.micromeritics.com/Repository/Files/mercury_paper.pdf.

[47] H. Giesche, Mercury Porosimetry: A General (Practical) Overview, Particle & Particle Systems Characterization. 23 (2006) 9–19. https://doi.org/10.1002/ppsc.200601009.

[48] W.K. Epting, J. Gelb, S. Litster, Resolving the three-dimensional microstructure of polymer electrolyte fuel cell electrodes using nanometer-scale x-ray computed

tomography, Advanced Functional Materials. 22 (2012) 555–560. https://doi.org/10.1002/adfm.201101525.

[49] L.G. de A. Melo, A.P. Hitchcock, V. Berejnov, D. Susac, J. Stumper, G.A. Botton, Evaluating focused ion beam and ultramicrotome sample preparation for analytical microscopies of the cathode layer of a polymer electrolyte membrane fuel cell, Journal of Power Sources. 312 (2016) 23–35. https://doi.org/10.1016/j.jpowsour.2016.02.019.

[50] C.-N. Sun, K.L. More, T.A. Zawodzinski, Investigation of transport properties, microstructure, and thermal behavior of PEFC catalyst layers, ECS Transactions. 33 (2010) 1207–1215. https://doi.org/10.1149/1.3484614.

[51] F. Xu, H. Zhang, J. Ilavsky, L. Stanciu, D. Ho, M.J. Justice, H.I. Petrache, J. Xie, Investigation of a catalyst ink dispersion using both ultra-small-angle x-ray scattering and cryogenic TEM, Langmuir. 26 (2012) 19199–19208. https://doi.org/10.1021/la1028228.

[52] E. Zschech, W. Yun, G. Schneider, High-resolution x-ray imaging - a powerful nondestructive technique for applications in semiconductor industry, Applied Physics A: Materials Science & Processing. 92 (2008) 423–429. https://doi.org/10.1007/s00339-008-4551-x.

[53] A. Tkachuk, F. Duewer, H.T. Cui, M. Feser, S. Wang, W.B. Yun, X-ray computed tomography in Zernike phase contrast mode at 8 keV with 50-nm resolution using Cu rotating anode X-ray source, Z. Kristall. 222 (2007) 650–655. https://doi.org/10.1524/zkri.2007.222.11.650.

[54] R.T. White, D. Ramani, S. Eberhardt, M. Najm, F.P. Orfino, M. Dutta, E. Kjeang, Correlative X-ray Tomographic Imaging of Catalyst Layer Degradation in Fuel Cells, Journal of The Electrochemical Society. 166 (2019) F914–F925. https://doi.org/10.1149/2.0121913jes.

[55] M. Andisheh-Tadbir, F.P. Orfino, E. Kjeang, Three-dimensional phase segregation of micro-porous layers for fuel cells by nano-scale X-ray computed tomography, Journal of Power Sources. 310 (2016) 61–69. https://doi.org/10.1016/j.jpowsour.2016.02.001.

[56] N. Yao, Focused Ion Beam Systems: Basics and Applications, Cambridge University Press, 2011. https://books.google.ca/books?id=N9nIRQAACAAJ.

[57] J.R. Wilson, J.S. Cronin, S.A. Barnett, S.J. Harris, Measurement of three-dimensional microstructure in a LiCoO2 positive electrode, Journal of Power Sources. 196 (2011) 3443–3447. https://doi.org/10.1016/j.jpowsour.2010.04.066.

[58] H. Iwai, N. Shikazono, T. Matsui, H. Teshima, M. Kishimoto, R. Kishida, D. Hayashi, K. Matsuzaki, D. Kanno, M. Saito, H. Muroyama, K. Eguchi, N. Kasagi, H. Yoshida, Quantification of SOFC anode microstructure based on dual beam FIB-SEM technique, Journal of Power Sources. 195 (2010) 955–961.

[59] H. Ostadi, P. Rama, Y. Liu, R. Chen, X.X. Zhang, K. Jiang, 3D reconstruction of a gas diffusion layer and a microporous layer, Journal of Membrane Science. 351 (2010) 69–74.

[60] A. Cecen, E.A. Wargo, A.C. Hanna, D.M. Turner, S.R. Kalidindi, E.C. Kumbur, 3-D microstructure analysis of fuel cell materials: spatial distributions of tortuosity, void size and diffusivity, Journal of The Electrochemical Society. 159 (2012) B299–B307. https://doi.org/10.1149/2.068203jes.

[61] M. Göbel, M. Godehardt, K. Schladitz, Multi-scale structural analysis of gas diffusion layers, Journal of Power Sources. 355 (2017) 8–17. https://doi.org/10.1016/j.jpowsour.2017.03.086.

[62] C.A. Volkert, A.M. Minor, Focused Ion Beam Microscopy and Micromachining, MRS Bulletin. 32 (2007) 389–399. https://doi.org/10.1557/mrs2007.62.

[63] E.A. Wargo, A.C. Hanna, A. Cecen, S.R. Kalidindi, E.C. Kumbur, Selection of representative volume elements for pore-scale analysis of transport in fuel cell materials, Journal of Power Sources. 197 (2012) 168–179.

[64] S. Kim, M.J. Park, N.P. Balsara, G. Liu, A.M. Minor, Minimization of focused ion beam damage in nanostructured polymer thin films, Ultramicroscopy. 111 (2011) 191–199. https://doi.org/10.1016/j.ultramic.2010.11.027.

[65] B.D. Lucas, Generalized Image Matching by the Method of Differences, PhD Thesis, Carnegie Mellon University, 1985.

[66] L. O'Gorman, M.J. Sammon, M. Seul, Practical algorithms for image analysis with CD-ROM, Cambridge University Press, 2008.

[67] S. Thiele, R. Zengerle, C. Ziegler, Nano-morphology of a polymer electrolyte fuel cell catalyst layer—imaging, reconstruction and analysis, Nano Research. 4 (2011). https://doi.org/10.1007/s12274-011-0141-x.

[68] T. Terao, G. Inoue, M. Kawase, N. Kubo, M. Yamaguchi, K. Yokoyama, T. Tokunaga, K. Shinohara, Y. Hara, T. Hara, Development of novel three-dimensional reconstruction method for porous media for polymer electrolyte fuel cells using focused ion beam-scanning electron microscope tomography, Journal of Power Sources. 347 (2017) 108–113. https://doi.org/10.1016/j.jpowsour.2017.02.050.

[69] Y. Mishchenko, A fast algorithm for computation of discrete Euclidean distance transform in three or more dimensions on vector processing architectures, Signal, Image and Video Processing. 9 (2015). https://doi.org/10.1007/s11760-012-0419-9.

[70] Y. Mishchenko, 3D euclidean distance transform for variable data aspect ratio, (2015). https://www.mathworks.com/matlabcentral/fileexchange/15455-3d-euclidean-distance-transform-for-variable-data-aspect-ratio (accessed August 4, 2021).

[71] K. Jiao, X. Li, Water transport in polymer electrolyte membrane fuel cells, Progress in Energy and Combustion Science. 37 (2011) 221–291.

[72] LiveLink™ for MATLAB® User's Guide, (2018). https://doc.comsol.com/5.4/doc/com.comsol.help.llmatlab/LiveLinkForMATLABUsersGuide.pdf.

[73] COMSOL Multiphysics Programming Reference Manual, (2018). https://doc.comsol.com/5.4/doc/com.comsol.help.comsol/COMSOL_ProgrammingReferenceManual.pdf.

[74] M.B. Clennell, Tortuosity: a guide through the maze, Geological Society, London, Special Publications. 122 (1997) 299. https://doi.org/10.1144/GSL.SP.1997.122.01.18.

[75] N. Epstein, On tortuosity and the tortuosity factor in flow and diffusion through porous media, Chemical Engineering Science. 44 (1989) 777–779. https://doi.org/10.1016/0009-2509(89)85053-5.

[76] D.A.G. Bruggeman, Calculation of various physics constants in heterogenous substances dielectricity constants and conductivity of mixed bodies from isotropic substances, Annalen Der Physik. 416 (1935) 636–664. https://doi.org/10.1002/andp.19354160705.

[77] B. Tjaden, D.J.L. Brett, P.R. Shearing, Tortuosity in electrochemical devices: a review of calculation approaches, Null. 63 (2018) 47–67. https://doi.org/10.1080/09506608.2016.1249995.

[78] P.R. Shearing, N.P. Brandon, J. Gelb, R. Bradley, P.J. Withers, A.J. Marquis, S. Cooper, S.J. Harris, Multi Length Scale Microstructural Investigations of a Commercially Available Li-Ion Battery Electrode, Journal of The Electrochemical Society. 159 (2012) A1023–A1027. https://doi.org/10.1149/2.053207jes.

[79] P.S. Jørgensen, S.L. Ebbehøj, A. Hauch, Triple phase boundary specific pathway analysis for quantitative characterization of solid oxide cell electrode microstructure, Journal of Power Sources. 279 (2015) 686–693. https://doi.org/10.1016/j.jpowsour.2015.01.054.

[80] S. Cooper, Quantifying the transport properties of solid oxide fuel cell electrodes, Imperial College London, 2015. https://spiral.imperial.ac.uk:8443/handle/10044/1/31600.

[81] K.T. Cho, M.M. Mench, Effect of material properties on evaporative water removal from polymer electrolyte fuel cell diffusion media, Journal of Power Sources. 195 (2010) 6748–6757.

[82] Z. Tayarani Yoosefabadi, Gas diffusion layer characterization and microstructural modeling in polymer electrolyte fuel cells, Simon Fraser University, 2021. https://summit.sfu.ca/item/21292 (accessed May 25, 2022).

[83] M.M. Tomadakis, S.V. Sotirchos, Ordinary and transition regime diffusion in random fiber structures, AIChE Journal. 39 (1993) 397–412. https://doi.org/10.1002/aic.690390304.

[84] X. Zhong, C.A. Wade, P.J. Withers, X. Zhou, C. Cai, S.J. Haigh, M.G. Burke, Comparing Xe+pFIB and Ga+FIB for TEM sample preparation of Al alloys: Minimising FIB-induced artefacts, Journal of Microscopy. 282 (2021) 101–112. https://doi.org/10.1111/jmi.12983.

[85] M.J. Eslamibidgoli, F.P. Tipp, J. Jitsev, J. Jankovic, M.H. Eikerling, K. Malek, Convolutional neural networks for high throughput screening of catalyst layer inks for polymer electrolyte fuel cells, RSC Adv. 11 (2021) 32126–32134. https://doi.org/10.1039/D1RA05324H.